

Thalamic reticular impairment underlies attention deficit in *Ptchd1*^{Y/-} mice

Michael F. Wells^{1,2*}, Ralf D. Wimmer^{3,4*}, L. Ian Schmitt^{3,4}, Guoping Feng^{2,5} & Michael M. Halassa^{3,4,6,7}

Developmental disabilities, including attention-deficit hyperactivity disorder (ADHD), intellectual disability (ID), and autism spectrum disorders (ASD), affect one in six children in the USA. Recently, gene mutations in patched domain containing 1 (*PTCHD1*) have been found in ~1% of patients with ID and ASD. Individuals with *PTCHD1* deletion show symptoms of ADHD, sleep disruption, hypotonia, aggression, ASD, and ID. Although *PTCHD1* is probably critical for normal development, the connection between its deletion and the ensuing behavioural defects is poorly understood. Here we report that during early post-natal development, mouse *Ptchd1* is selectively expressed in the thalamic reticular nucleus (TRN), a group of GABAergic neurons that regulate thalamocortical transmission, sleep rhythms, and attention. *Ptchd1* deletion attenuates TRN activity through mechanisms involving small conductance calcium-dependent potassium currents (SK). TRN-restricted deletion of *Ptchd1* leads to attention deficits and hyperactivity, both of which are rescued by pharmacological augmentation of SK channel activity. Global *Ptchd1* deletion recapitulates learning impairment, hyper-aggression, and motor defects, all of which are insensitive to SK pharmacological targeting and not found in the TRN-restricted deletion mouse. This study maps clinically relevant behavioural phenotypes onto TRN dysfunction in a human disease model, while also identifying molecular and circuit targets for intervention.

Recent genetic studies have revealed substantial overlap of risk genes across seemingly distinct neurodevelopmental and psychiatric disorders including ASD, ADHD, schizophrenia, and ID¹⁻⁴. Such shared genetic architectures could potentially explain the overlap of behavioural abnormalities across these diagnostic categories, but because of the difficulty in mapping circuitry mechanisms of behaviour, understanding how diverse genetic lesions converge onto behaviour-relevant circuit dysfunction has been limited.

Here we focused on *PTCHD1*, a gene that is mutated in about 1% of all patients with ASD and ID⁵⁻¹⁰. Comprehensive clinical analysis of *PTCHD1* deletion patients identified a variable non-syndromic neurodevelopmental disorder with symptoms ranging from attention deficit, hyperactivity, sleep abnormality, hypotonia, and learning disability¹¹. We found that *Ptchd1* was selectively expressed in the TRN of mice in early development and continued to be enriched in this structure throughout adult life. The TRN is critical for thalamocortical transmission¹²⁻¹⁵, generation of sleep rhythms^{12,16-18}, sensorimotor processing^{19,20}, and attention^{13,21}, and its perturbation could result in deficits in these domains. By generating a conditional *Ptchd1*-knockout mouse, we mapped ADHD-like behaviours onto TRN circuit dysfunction via two independent methods. First, by deleting *Ptchd1* selectively from the TRN, we replicated the attention deficit and hyperactivity behaviours, but not other disease-related phenotypes found in the full knockout. Second, pharmacological rescue of TRN biophysical dysfunction selectively rescued these ADHD-related behaviours in the *Ptchd1* knockout. These findings constitute the first evidence for a 'leaky thalamus' in a neurodevelopmental disorder, where irrelevant inputs that are normally suppressed become highly distracting. Most importantly, we identified the TRN and its SK channels as circuit and molecular targets for intervention.

Altered TRN neuronal biophysics

The X-linked *Ptchd1* gene is predicted to encode a twelve-pass transmembrane protein with a sterol-sensing domain⁵, prompting its classification as a member of the Patched family and speculation that it may function as a Sonic hedgehog receptor²²⁻²⁴. Prenatally, *Ptchd1* expression is found in the developing cerebellum and diencephalon (http://www.ncbi.nlm.nih.gov/nucore/NM_001093750). We found *Ptchd1* mRNA to be confined to the TRN at birth, and by post-natal day 15 (P15) onwards, to be expressed in the striatum, cortex, and cerebellum (Fig. 1a, b, Extended Data Fig. 1, Supplementary Table 1). Interestingly, Patched family members *Ptchd2* and *Ptchd3* show no TRN expression (<http://www.brain-map.org/>, 77620810 and 71891731, respectively). Thus, *Ptchd1* may play a unique role in the TRN.

To understand how *Ptchd1* deletion might contribute to neurodevelopmental disorders, we generated a conditional allele of *Ptchd1* by targeting exon 2 (Extended Data Fig. 2a). This exon encodes 3 out of the 12 transmembrane domains, including a substantial portion of the sterol-sensing domain. Loss of this exon is predicted to generate a prematurely terminated non-functional protein (Extended Data Fig. 2b). *In situ* hybridization, genotype PCR, and cDNA transcript analyses confirmed successful excision of exon 2 (Extended Data Fig. 2c-e; for source data, see Supplementary Fig. 1). Because *Ptchd1* is X-linked and individuals with *PTCHD1* deletion are almost exclusively males, we used hemizygous male mice (*Ptchd1*^{Y/-}; referred to as *Ptchd1*-knockout) for this study. *Ptchd1*-knockout mice were viable with normal body weight allowing for direct genetic modelling of this human condition.

Given the enriched expression of *Ptchd1* in the TRN, we focused our initial investigation on this structure in *Ptchd1*-knockout mice. The TRN is a group of GABAergic neurons that provide the major source of inhibition to thalamic relay nuclei, and are thought to regulate cortical

¹Department of Neurobiology, Duke University Medical Center, Durham, North Carolina 27710, USA. ²McGovern Institute for Brain Research, Department of Brain and Cognitive Sciences, Massachusetts Institute of Technology, Cambridge, Massachusetts 02139, USA. ³Neuroscience Institute, New York University Langone Medical Center, New York, New York 10016, USA.

⁴Department of Neuroscience and Physiology, New York University Langone Medical Center, New York, New York 10016, USA. ⁵Stanley Center for Psychiatric Research, Broad Institute of MIT and Harvard, Cambridge, Massachusetts 02142, USA. ⁶Department of Psychiatry, New York University Langone Medical Center, New York, New York 10016, USA. ⁷Center for Neural Science, New York University, New York, New York 10003, USA.

*These authors contributed equally to this work.

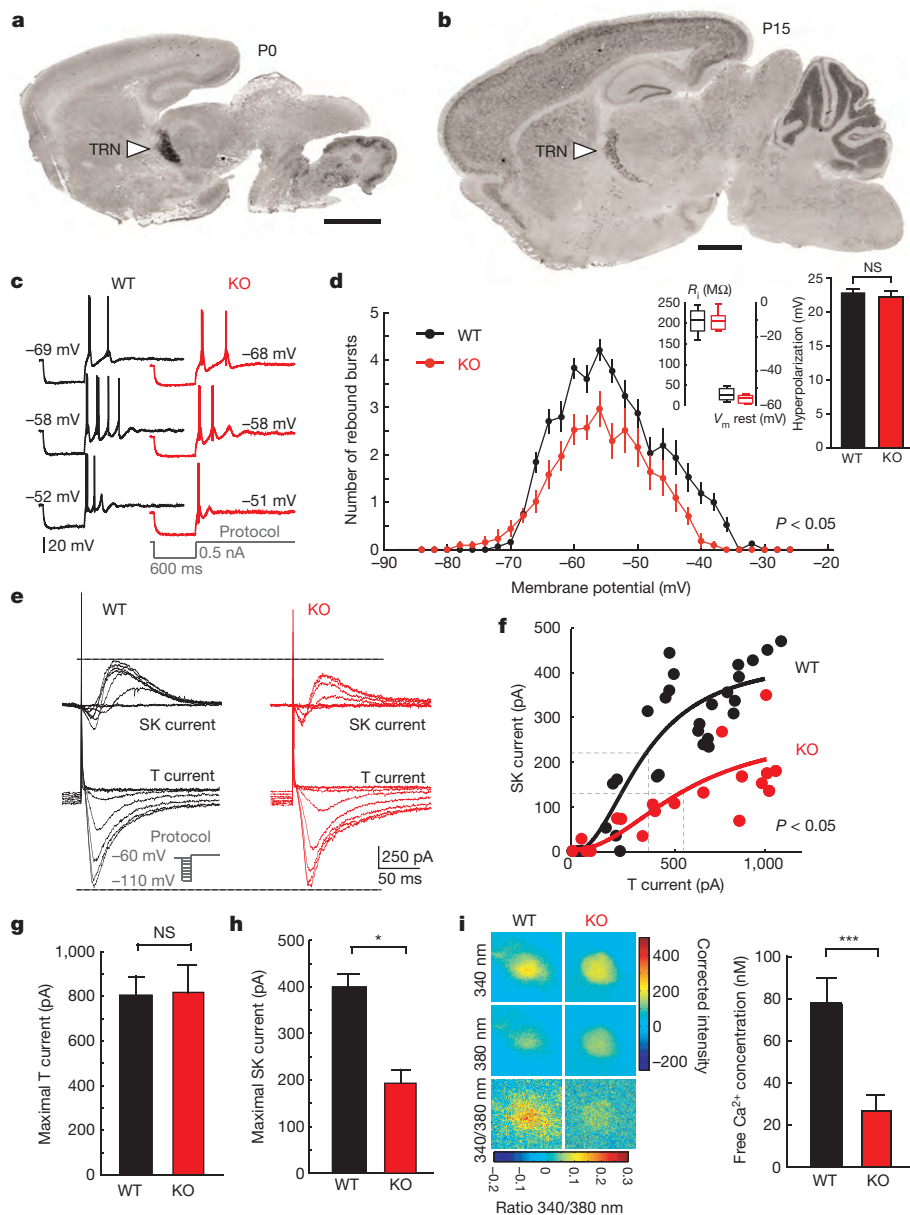


Figure 1 | Impaired repetitive bursting and SK2 currents in TRN neurons from knockout mice. **a, b,** *Ptchd1* expression ($n = 3$ wild-type (WT) mice). Scale bar, 1 mm. **c,** Representative TRN burst traces ($n = 8$ WT, 9 KO cells). **d,** Reduced burst firing in knockout (KO) TRN neurons ($n = 8$ WT, 9 KO cells). V_m rest, resting membrane potential; R_i , input resistance. **e,** Representative T and SK2 current traces. **f–h,** Normal T (**g**) and reduced SK2 currents (**h**) in knockout cells ($n = 8$ WT, 9 KO). **i,** Diminished free $[Ca^{2+}]_i$ in knockout cells. Representative heat maps show background-corrected intensity ($n = 37$ WT, 36 KO cells). Wilcoxon rank-sum (**d, f–h**) and two-tailed *t*-tests (**i**). Error bars, mean \pm s.e.m. * $P < 0.05$; *** $P < 0.001$; NS, not significant.

rhythms, sleep, and attention^{21,25,26}. To begin investigating possible physiological changes in the knockout mice, we exploited a well-known characteristic of TRN neurons. Depending on their resting membrane potential, these neurons fire in two distinct modes upon receiving synaptic input²⁷. At depolarized membrane potential, they fire tonic Na^+ spikes. When hyperpolarized, they generate repetitive 'low-threshold' Ca^{2+} transients crowned by high-frequency Na^+ spikes known as bursts^{26,28–30}. Whole-cell patch-clamp recordings of TRN neurons revealed a significant decrease in repetitive bursting in knockout mice compared to wild-type controls (Fig. 1c, d). These changes were not the result of altered knockout TRN neuron resting membrane potential, input resistance, or escape from hyperpolarization (Fig. 1d, inset).

Because repetitive bursting is known to depend on interactions between T-type Ca^{2+} and small conductance calcium-activated K^+ channels²⁶, we asked which of these two conductances were primarily impaired in the knockout mice. Under voltage clamp, we found that T currents were intact but SK currents were reduced by 50% in the knockout (Fig. 1e–h). As SK channels are sensitive to resting state intracellular Ca^{2+} ($[Ca^{2+}]_i$)^{26,31}, we measured this concentration using the ratiometric Ca^{2+} indicator Fura-2AM in TRN neurons from acute brain slices. We found a twofold reduction of $[Ca^{2+}]_i$ in knockout

TRN neurons (Fig. 1i), suggesting that altered Ca^{2+} homeostasis may underlie SK channel deficits.

Reduced TRN-generated sleep spindles

Previous studies have suggested that TRN bursting plays a role in the generation of sleep spindles^{19,28}, predicting that the diminished bursting found in *Ptchd1*-knockout mice would lead to reduced sleep spindles. Using independently adjustable multi-electrode arrays to directly target TRN neurons for electrophysiological recordings in freely behaving animals and surface electroencephalography (Fig. 2a, Extended Data Fig. 3a)³², we discovered that TRN neurons from knockout mice exhibited reduced burst firing in sleep (Fig. 2b) and knockout mice showed an overall reduction in sleep spindle count (Fig. 2c, Extended Data Fig. 3b, c). Further, the degree of TRN neuronal engagement in spindle events was substantially diminished in the knockout (Extended Data Fig. 3d–f), supporting the link between the cellular and network phenotypes in this disorder and perhaps other human neurodevelopmental disorders^{33,34}. Importantly, consistent with the notion that sleep spindles are a marker for sleep stability^{35,36}, we found *Ptchd1*-knockout mice to display highly fragmented sleep (Fig. 2d–f, Supplementary Table 2).

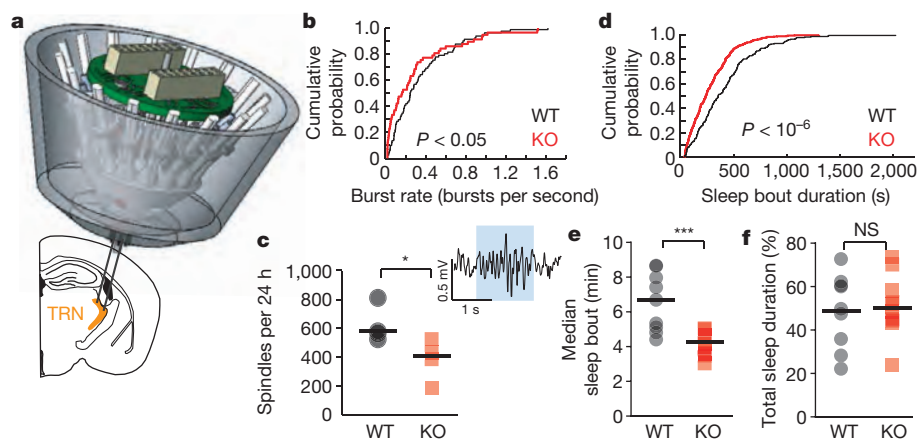


Figure 2 | Decreased spindles and sleep fragmentation in knockout mice

a, Multi-electrode implant targeting TRN. **b**, Decreased TRN burst discharge in knockouts ($n = 89$ WT, 80 KO cells from 4 WT, 3 KO mice). **c**, Reduced spindles in knockout mice. **d–f**, Knockout mice display shorter sleep bouts with normal total sleep duration ($n = 9$ WT, 10 KO). Kolmogorov–Smirnov (**b**, **d**) and Wilcoxon rank-sum tests (**c**, **e–f**). Horizontal, median (**c**, **e–f**). * $P < 0.05$; *** $P < 0.001$.

Impaired sensory-evoked thalamic inhibition

In addition to reduced rebound bursting, insufficient K^+ -mediated hyperpolarization is expected to more generally alter TRN neuronal excitability. Most importantly, it could lead to neurons not being hyperpolarized enough for T-type Ca^{2+} channels to de-inactivate and boost excitability²⁴. Therefore, despite finding T-type currents to be intact under controlled voltage-clamp conditions (at -70 mV), insufficient hyperpolarization caused by reduced SK currents would render T-type channels less recruitable under physiological conditions¹⁷, leading to reduced TRN neuronal activity and diminished overall thalamic inhibition. To test this prediction at the population level and in the intact brain, we used chloride photometry, a tool that we recently developed as a proxy for population-level GABAergic inhibition¹³. This technique utilizes fluorescence resonance energy transfer (FRET)-based measurements of the chloride-sensor SuperClomeleon³⁷, a reporter composed of a cyan fluorescent protein (CFP) FRET-donor and a chloride-quenchable yellow fluorescent protein (YFP) FRET acceptor (Fig. 3a). By introducing SuperClomeleon into visual thalamic neurons (lateral geniculate nucleus, LGN; Fig. 3b), we observed visual-evoked chloride transients (Fig. 3c, d), replicating our recent findings¹³. Visual-evoked inhibitory transients were observed in both wild-type and *Ptchd1*-knockout LGN, but a quantitative comparison revealed a 25% reduction of these transients in

the knockout (Fig. 3e–g). Impaired inhibition was also observed in response to trains of stimuli (Fig. 3h, j). Interestingly, a small inhibitory augmentation as a result of repeated stimulation was observed in wild-type mice and this augmentation was also significantly reduced in the knockouts (Fig. 3h, i). Altogether, these findings provide direct evidence for reduced thalamic inhibition in *Ptchd1*-knockout mice and are consistent with impaired TRN output with ensuing deficits in sensory-related thalamic inhibition.

ADHD-like behaviours in *Ptchd1*-knockout mice

We have previously observed that thalamic inhibition is used to suppress unwanted sensory inputs during attention¹². The observed reduction in thalamic inhibition (Fig. 3) would predict that unwanted sensory inputs may become particularly distracting for *Ptchd1*-knockout mice. To test this hypothesis, we trained mice on a visual detection task shown to require attentional engagement¹² (Fig. 4a). Mice initiated each trial by continuously breaking an infrared barrier for 0.5–0.7 s, ensuring proper head position when a visual stimulus was presented either to the right or left of the animal. Correct indication of visual stimulus location by nose-poking resulted in reward delivery. Under such conditions, *Ptchd1*-knockout mice performance was comparable to that of a wild type (Fig. 4b). However, in the presence of a visual distractor during anticipation, knockout mice showed impaired

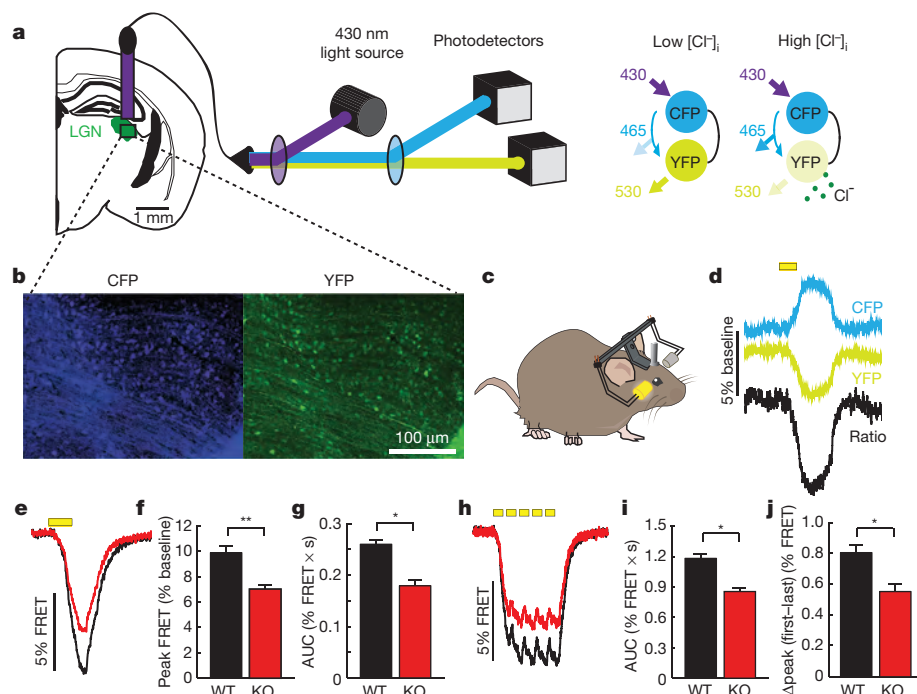
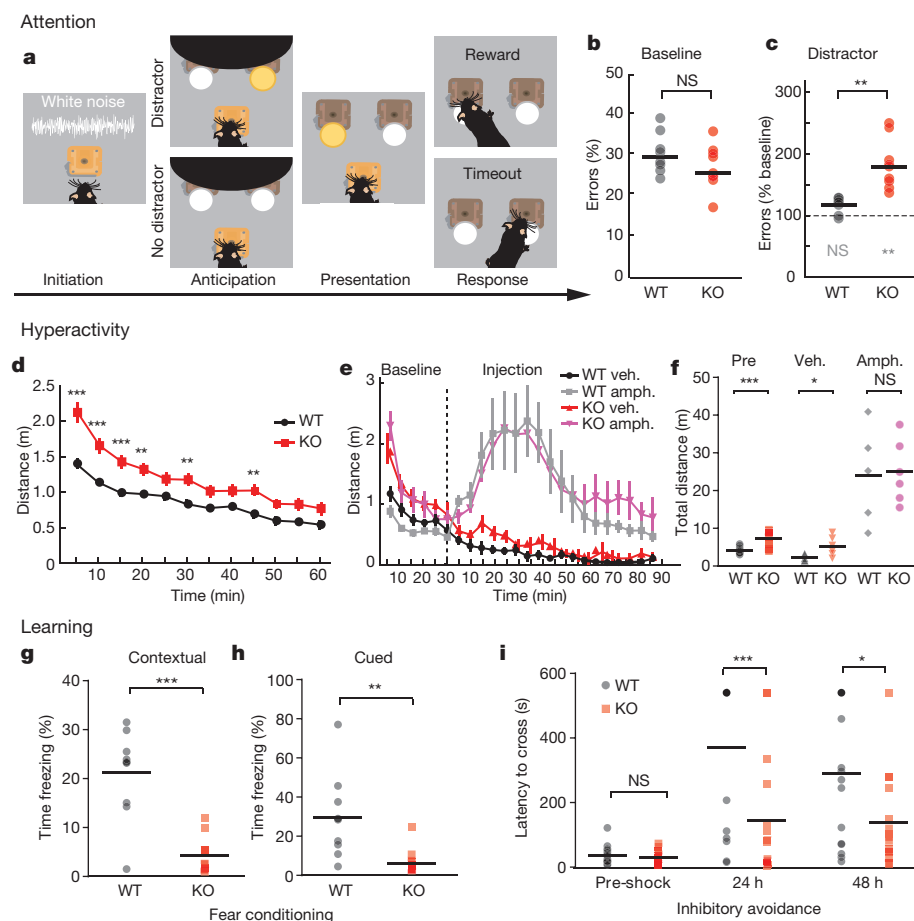


Figure 3 | Reduced sensory-evoked thalamic inhibition in knockout mice.

a, Schematic of CFP to YFP FRET. **b**, Confocal images of SuperClomeleon expression in LGN. **c**, Stimuli delivered to the eye contralateral to implanted LGN. **d**, Example traces of visual-evoked CFP and YFP fluorescence changes. **e–g**, Reduced LGN inhibition in knockouts, reflected in peak FRET response (**f**) and smaller area under the curve (AUC; **g**). **h–j**, Knockout mice also show decreased facilitation of FRET response. $n = 6$ WT, 6 KO mice. Wilcoxon rank-sum tests (**e–j**). Error bars, mean \pm s.e.m. * $P < 0.05$; ** $P < 0.01$.



performance (Fig. 4c). The specific distractibility phenotype, rather than a more general failure of attentional engagement, revealed by this novel behavioural task is consistent with the prediction of impaired thalamic inhibition required for distractor suppression. It is also consistent with clinical findings in patients with related neurodevelopmental disorders³⁸. This impairment was not the result of general sensorimotor dysfunction, given the intact performance on standard sensorimotor testing (Extended Data Fig. 4a–c).

Distractibility is often accompanied by hyperactivity in several human neurodevelopmental disorders such as ADHD^{39,40}. ADHD symptoms are frequently observed in patients with *PTCHD1* mutations¹¹. Interestingly, *Ptchd1*-knockout mice showed a hyperactivity phenotype in the open field (Fig. 4d). Classical ADHD-related hyperactivity is predicted to be treated effectively with amphetamines, as has been previously described in other mouse models of neurodevelopmental disease⁴¹. Surprisingly, *Ptchd1*-knockout hyperactivity was insensitive to amphetamine treatment (Fig. 4e, f), suggesting a unique pathophysiological origin that may be related to the approximately 30% of ADHD patients who do not respond to amphetamines⁴².

In addition to attention deficits and hyperactivity, *Ptchd1*-knockout mice showed a variety of behavioural abnormalities. Although knockout mice showed intact performance on tasks requiring simple spatial learning (Extended Data Fig. 5a–d), they exhibited significant deficits on tasks necessitating more complex associations that are believed to require integration across multiple brain structures⁴³. Knockout mice showed fear-induced freezing deficits in contextual (Fig. 4g) and cued (Fig. 4h) fear-conditioning tests. Impaired learning was corroborated by profound deficits on the inhibitory avoidance task (Fig. 4i). Knockout mice also exhibited motor defects such as gait abnormalities and hypotonia, as well as hyper-aggression (Extended Data Fig. 5e–h). All of these behaviours were independent of genetic background (Extended Data Fig. 6). These behaviours are consistent with clinical

findings of multi-system abnormalities in *PTCHD1* deletion patients, suggesting the major function of *PTCHD1* is evolutionarily conserved. Interestingly, although several *PTCHD1* deletion patients have been diagnosed with ASD, knockout mice did not exhibit differences in repetitive grooming (Extended Data Fig. 7a) or social interaction (Extended Data Fig. 7b, c). This may reflect evolutionary divergence either in *PTCHD1* function or in behavioural circuits related to *PTCHD1* deficiency⁴⁴.

TRN defects underlie ADHD-like behaviours

To determine which behavioural abnormalities are caused by TRN dysfunction, we sought strategies to largely limit *Ptchd1* deletion to the TRN. To choose the appropriate Cre-driver line to breed with floxed *Ptchd1* (*Ptchd1*^{+/*fl*}) mice, we looked for specific TRN overlap between candidate markers and *PTCHD1* expression. Immunohistochemical co-labelling experiments of *Ptchd1*-YFP^{+/-}, a novel knock-in mouse with yellow fluorescent protein (YFP) in place of *Ptchd1* exon 1 (Extended Data Fig. 8a), revealed significant and unique overlap between YFP and the inhibitory neuronal marker GAD67 in the TRN (Extended Data Fig. 8b, Supplementary Table 3).

Both parvalbumin and somatostatin are inhibitory neural markers that are widely expressed across TRN neurons^{45,46} and showed overlap with YFP limited to this region (Extended Data Fig. 8c), suggesting that mating Cre-drivers of either parvalbumin or somatostatin to *Ptchd1*^{+/*fl*} mice would result in a *Ptchd1* deletion that is primarily confined to the TRN. Given the early post-natal expression of *PTCHD1* and somatostatin in the TRN (Extended Data Fig. 9), we reasoned that knock-in mice expressing Cre recombinase in somatostatin neurons without disrupting endogenous *Sst* expression (*Sst*-Cre) would be a more suitable choice for such experiments⁴⁷. We crossed *Ptchd1*^{+/*fl*} female mice to *Sst*-Cre mice and generated male lacking *Ptchd1* in the TRN (*Sst*-Cre⁺ *Ptchd1*^{Y/*fl*}), as confirmed by *in situ* hybridization (Fig. 5a).

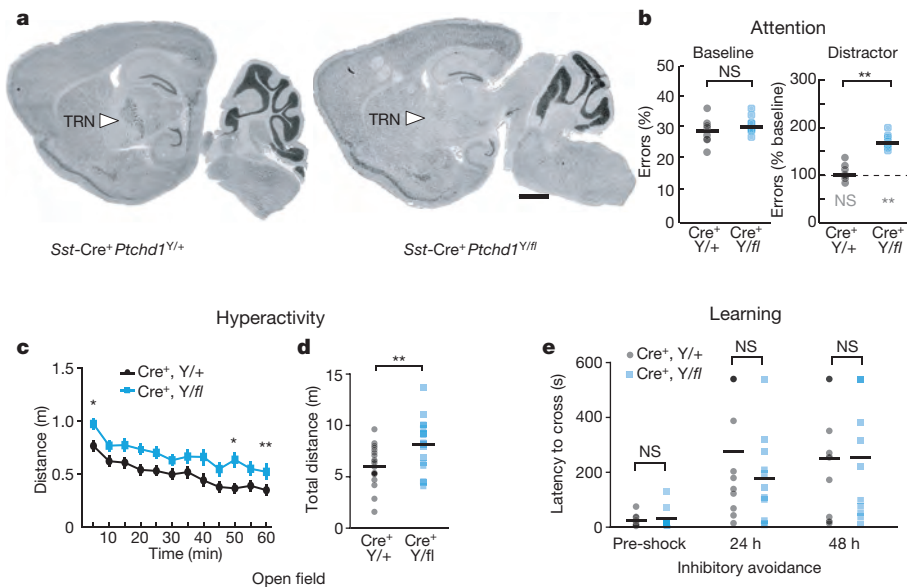


Figure 5 | TRN dysfunction explains ADHD-like behaviours in knockout mice. **a**, *Ptchd1* ablation from TRN (scale bar, 1 mm). **b**, *Sst-Cre⁺Ptchd1^{Y/fl}* mice recapitulate attention deficits observed in knockouts ($n = 8 Ptchd1^{Y/+}$, $8 Ptchd1^{Y/fl}$). Dashed line, baseline performance (without distractors). **c**, **d**, *Sst-Cre⁺Ptchd1^{Y/fl}* mice are hyperactive ($n = 21 Ptchd1^{Y/+}$, $22 Ptchd1^{Y/fl}$). **e**, *Sst-Cre⁺Ptchd1^{Y/fl}* mice show intact ability to form complex association ($n = 11 Ptchd1^{Y/+}$, $12 Ptchd1^{Y/fl}$). Wilcoxon rank-sum (**b**), two-tailed *t*-test (**d**), and two-way reduced measures ANOVA with Bonferroni post-hoc tests (**c**, **e**). Error bars, mean \pm s.e.m. (**c**); horizontal bars, mean (**d**, **e**). * $P < 0.05$; ** $P < 0.01$; NS, not significant (grey asterisks in **b** indicate statistical difference compared to baseline performance).

Sst-Cre⁺Ptchd1^{Y/fl} mice displayed attention deficits (Fig. 5b) and recapitulated the hyperactivity phenotype observed in the germline knockout (Fig. 5c, d), suggesting that these behaviours are explained by TRN dysfunction. *Sst-Cre⁺Ptchd1^{Y/fl}* mice showed intact learning (Fig. 5e) and did not show hypotonia or hyper-aggression (Extended Data Fig. 10a, b), reaffirming the circuit specificity of this genetic model. Interestingly, *Sst-Cre⁺Ptchd1^{Y/fl}* mice exhibited fragmented sleep (Extended Data Fig. 10c–e), confirming the notion that sleep abnormalities observed in the germline knockout are of TRN origin, and that sleep and attention deficits can arise from common circuit dysfunction⁴⁸.

Finally, we asked whether pharmacological boosting of SK channels could rescue ADHD-like knockout behaviours. Acute injection of the SK positive allosteric modulator 1-ethyl-benzimidazolone (1-EBIO) significantly mitigated impaired sensory-evoked thalamic inhibition in germline knockout mice with no impact on inhibitory transients in the wild types (Fig. 6a). Consistent with these physiological effects, 1-EBIO did not affect attentional task performance in the wild-type mice (Fig. 6b), but substantially mitigated distractibility in the knockout mice (Fig. 6c). In addition, 1-EBIO injection rescued the hyperactivity phenotype in the knockouts (Fig. 6d, e). The specificity of this pharmacological approach was supported by its lack of effect on other abnormalities including hypotonia (Extended Data Fig. 10f),

hyper-aggression (Extended Data Fig. 10g), and learning deficits (Fig. 6f). Together, these results further support SK channel dysfunction as a cellular mechanism for these behavioural abnormalities. Future studies examining the therapeutic benefit of SK targeting for sleep fragmentation and instability and its potential relevance to inattention would be important.

Discussion

To our knowledge, this study is the first to show that a TRN circuit deficit is central to a specific set of behavioural impairments in a human neurodevelopmental disease model. Using conditional knockout of *Ptchd1*, a gene with expression restricted to the TRN during early post-natal development, we mapped behavioural phenotypes onto their circuit substrates. We additionally discovered that modulation of SK channel function could be explored as a potential novel treatment strategy for *PTCHD1* deletion patients with attention deficits and hyperactivity. Hyperactivity of TRN origin may be the motor equivalent of sensory distractibility, which could involve dysfunctional motor TRN-thalamic circuits. Future experiments exploring inhibitory control of motor thalamus will formally test this conjecture.

Although basic studies have shown the TRN to be central for attention^{21,49} and sleep spindles¹⁶, our study directly shows how disease-relevant impaired TRN output can result in attention deficits,

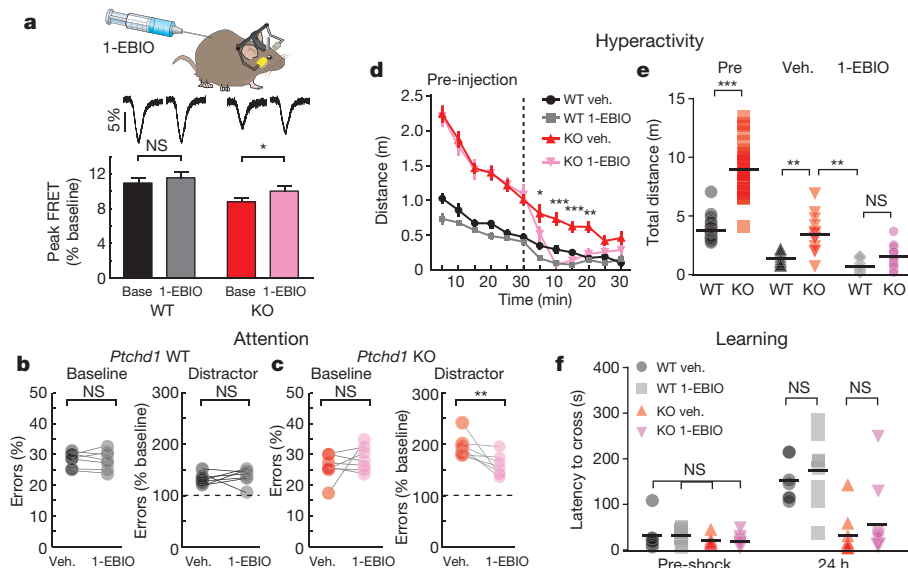


Figure 6 | SK conductance augmentation corrects ADHD-like symptoms in knockout mice. **a**, 1-EBIO corrects inhibitory transients in knockouts ($n = 7$ WT veh., 7 1-EBIO-treated WT (WT 1-EBIO), 7 KO veh., 7 KO 1-EBIO). **b**, **c**, 1-EBIO improves attention performance in knockout mice ($n = 7$ WT veh., 7 WT 1-EBIO, 7 KO veh., 7 KO 1-EBIO). Dashed lines, baseline performance; grey bars connect data points from the same animal. **d**, **e**, 1-EBIO rescues hyperactivity in knockouts ($n = 13$ WT veh., 13 WT 1-EBIO, 13 KO veh., 15 KO 1-EBIO). **f**, Treatment with 1-EBIO did not affect inhibitory avoidance ($n = 7$ WT veh., 8 WT 1-EBIO, 9 KO veh., 10 KO 1-EBIO). Wilcoxon rank-sum (**a**–**c**) and two-way reduced measures ANOVA with Bonferroni post-hoc tests (**d**–**f**). Error bars, mean \pm s.e.m. (**a**, **d**); horizontal bars, mean (**e**, **f**). * $P < 0.05$; ** $P < 0.01$; *** $P < 0.001$.

hyperactivity, and sleep disruption. This direct demonstration was made possible by developing SuperClomeleon photometry, a technique that can now be widely applied to disease models as a screen for impaired thalamic inhibition. It is possible that a 'leaky thalamus' caused by impaired TRN function underlies attention deficits, hyperactivity, and sleep disruption across various neurodevelopmental disorders, and we expect the set of genetic, physiologic, and behavioural approaches we introduce here to facilitate such discoveries.

Online Content Methods, along with any additional Extended Data display items and Source Data, are available in the online version of the paper; references unique to these sections appear only in the online paper.

Received 20 October 2015; accepted 17 February 2016.

Published online 23 March 2016.

- Coe, B. P., Girirajan, S. & Eichler, E. E. The genetic variability and commonality of neurodevelopmental disease. *Am. J. Med. Genet. C. Semin. Med. Genet.* **160C**, 118–129 (2012).
- Coe, B. P., Girirajan, S. & Eichler, E. E. A genetic model for neurodevelopmental disease. *Curr. Opin. Neurobiol.* **22**, 829–836 (2012).
- Zhou, Y. *et al.* Mice with *Shank3* mutations associated with ASD and schizophrenia display both shared and distinct defects. *Neuron* **89**, 147–162 (2016).
- Cristino, A. S. *et al.* Neurodevelopmental and neuropsychiatric disorders represent an interconnected molecular system. *Mol. Psychiatry* **19**, 294–301 (2014).
- Noor, A. *et al.* Disruption at the *PTCHD1* locus on Xp22.11 in Autism spectrum disorder and intellectual disability. *Sci. Transl. Med.* **2**, 49ra68 (2010).
- Pinto, D. *et al.* Functional impact of global rare copy number variation in autism spectrum disorders. *Nature* **466**, 368–372 (2010).
- Whibley, A. C. *et al.* Fine-scale survey of X chromosome copy number variants and indels underlying intellectual disability. *Am. J. Hum. Genet.* **87**, 173–188 (2010).
- Marshall, C. R. *et al.* Structural variation of chromosomes in autism spectrum disorder. *Am. J. Hum. Genet.* **82**, 477–488 (2008).
- Filges, I. *et al.* Deletion in Xp22.11: *PTCHD1* is a candidate gene for X-linked intellectual disability with or without autism. *Clin. Genet.* **79**, 79–85 (2011).
- Torricco, B. *et al.* Contribution of common and rare variants of the *PTCHD1* gene to autism spectrum disorders and intellectual disability. *Eur. J. Hum. Genet.* **23**, 1694–1701 (2015).
- Chaudhry, A. *et al.* Phenotypic spectrum associated with *PTCHD1* deletions and truncating mutations includes intellectual disability and autism spectrum disorder. *Clin. Genet.* **88**, 224–233 (2015).
- Halassa, M. M. *et al.* State-dependent architecture of thalamic reticular subnetworks. *Cell* **158**, 808–821 (2014).
- Wimmer, R. D. *et al.* Thalamic control of sensory selection in divided attention. *Nature* **526**, 705–709 (2015).
- Pinault, D. The thalamic reticular nucleus: structure, function and concept. *Brain Res. Brain Res. Rev.* **46**, 1–31 (2004).
- Guillery, R. W., Feig, S. L. & Lozsadi, D. A. Paying attention to the thalamic reticular nucleus. *Trends Neurosci.* **21**, 28–32 (1998).
- Halassa, M. M. *et al.* Selective optical drive of thalamic reticular nucleus generates thalamic bursts and cortical spindles. *Nature Neurosci.* **14**, 1118–1120 (2011).
- Barthó, P. *et al.* Ongoing network state controls the length of sleep spindles via inhibitory activity. *Neuron* **82**, 1367–1379 (2014).
- von Krosigk, M., Bal, T. & McCormick, D. A. Cellular mechanisms of a synchronized oscillation in the thalamus. *Science* **261**, 361–364 (1993).
- Marlinski, V., Sirota, M. G. & Beloozerova, I. N. Differential gating of thalamocortical signals by reticular nucleus of thalamus during locomotion. *J. Neurosci.* **32**, 15823–15836 (2012).
- Erlj, D. *et al.* Dopamine D4 receptor stimulation in GABAergic projections of the globus pallidus to the reticular thalamic nucleus and the substantia nigra reticulata of the rat decreases locomotor activity. *Neuropharmacology* **62**, 1111–1118 (2012).
- McAlonan, K., Cavanaugh, J. & Wurtz, R. H. Guarding the gateway to cortex with attention in visual thalamus. *Nature* **456**, 391–394 (2008).
- Zhong, Y. *et al.* Comprehensive analysis of patched domain-containing genes reveals a unique evolutionary pattern. *Genet. Mol. Res.* **13**, 7318–7331 (2014).
- Goodrich, L. V. *et al.* Altered neural cell fates and medulloblastoma in mouse patched mutants. *Science* **277**, 1109–1113 (1997).
- Rohatgi, R., Milenkovic, L. & Scott, M. P. Patched1 regulates hedgehog signaling at the primary cilium. *Science* **317**, 372–376 (2007).
- Jasper, H. Diffuse projection systems: the integrative action of the thalamic reticular system. *Electroencephalogr. Clin. Neurophysiol.* **1**, 405–419 (1949).
- Cueni, L. *et al.* T-type Ca²⁺ channels, SK2 channels and SERCAs gate sleep-related oscillations in thalamic dendrites. *Nature Neurosci.* **11**, 683–692 (2008).
- Jahnsen, H. & Llinas, R. Voltage-dependent burst-to-tonic switching of thalamic cell activity: an in vitro study. *Arch. Ital. Biol.* **122**, 73–82 (1984).
- Astori, S. *et al.* The Ca(V)_{3.3} calcium channel is the major sleep spindle pacemaker in thalamus. *Proc. Natl Acad. Sci. USA* **108**, 13823–13828 (2011).
- Huguenard, J. R. & Prince, D. A. A novel T-type current underlies prolonged Ca(2+)-dependent burst firing in GABAergic neurons of rat thalamic reticular nucleus. *J. Neurosci.* **12**, 3804–3817 (1992).
- Ying, S. W. & Goldstein, P. A. Propofol-block of SK channels in reticular thalamic neurons enhances GABAergic inhibition in relay neurons. *J. Neurophysiol.* **93**, 1935–1948 (2005).
- Coulon, P. *et al.* Burst discharges in neurons of the thalamic reticular nucleus are shaped by calcium-induced calcium release. *Cell Calcium* **46**, 333–346 (2009).
- Brunetti, P. M. *et al.* Design and fabrication of ultralight weight, adjustable multi-electrode probes for electrophysiological recordings in mice. *J. Vis. Exp.* **91**, e51675 (2014).
- Ferrarelli, F. *et al.* Reduced sleep spindle activity in schizophrenia patients. *Am. J. Psychiatry* **164**, 483–492 (2007).
- Limoges, E. *et al.* Atypical sleep architecture and the autism phenotype. *Brain* **128**, 1049–1061 (2005).
- Dang-Vu, T. T. *et al.* Spontaneous brain rhythms predict sleep stability in the face of noise. *Curr. Biol.* **20**, R626–R627 (2010).
- Wimmer, R. D. *et al.* Sustaining Sleep Spindles through Enhanced SK2-Channel Activity Consolidates Sleep and Elevates Arousal Threshold. *J. Neurosci.* **32**, 13917–13928 (2012).
- Grimley, J. S. *et al.* Visualization of synaptic inhibition with an optogenetic sensor developed by cell-free protein engineering automation. *J. Neurosci.* **33**, 16297–16309 (2013).
- Remington, A. *et al.* Selective attention and perceptual load in autism spectrum disorder. *Psychol. Sci.* **20**, 1388–1393 (2009).
- Sachs, G. S. *et al.* Comorbidity of attention deficit hyperactivity disorder with early- and late-onset bipolar disorder. *Am. J. Psychiatry* **157**, 466–468 (2000).
- Leyfer, O. T. *et al.* Comorbid psychiatric disorders in children with autism: interview development and rates of disorders. *J. Autism Dev. Disord.* **36**, 849–861 (2006).
- Won, H. *et al.* GIT1 is associated with ADHD in humans and ADHD-like behaviors in mice. *Nature Med.* **17**, 566–572 (2011).
- Spencer, T. *et al.* Efficacy of a mixed amphetamine salts compound in adults with attention-deficit/hyperactivity disorder. *Arch. Gen. Psychiatry* **58**, 775–782 (2001).
- Curzon, P., Rustay, N. R. & Browman, K. E. In *Methods of Behavior Analysis in Neuroscience* 2nd edn (ed. Buccafusco, J. J.) Ch. 2 (Boca Raton, 2009).
- Nestler, E. J. & Hyman, S. E. Animal models of neuropsychiatric disorders. *Nature Neurosci.* **13**, 1161–1169 (2010).
- Meyer, A. H. *et al.* In vivo labeling of parvalbumin-positive interneurons and analysis of electrical coupling in identified neurons. *J. Neurosci.* **22**, 7055–7064 (2002).
- Graybiel, A. M. & Elde, R. P. Somatostatin-like immunoreactivity characterizes neurons of the nucleus reticularis thalami in the cat and monkey. *J. Neurosci.* **3**, 1308–1321 (1983).
- Taniguchi, H. *et al.* A resource of Cre driver lines for genetic targeting of GABAergic neurons in cerebral cortex. *Neuron* **71**, 995–1013 (2011).
- Chen, Z. *et al.* Thalamic circuit mechanisms link sensory processing in sleep and attention. *Front. in Neural Circuits* <http://dx.doi.org/10.3389/fncir.2015.00083> (2015).
- Zikopoulos, B. & Barbas, H. Pathways for emotions and attention converge on the thalamic reticular nucleus in primates. *J. Neurosci.* **32**, 5338–5350 (2012).

Supplementary Information is available in the online version of the paper.

Acknowledgements We thank R. Tang for insightful discussion during the initiation of the project, H. Wang, T. Dalia, E. Kwan, H. Zaniwski for technical support, and J. Vincent for insightful discussion. We thank J. Petravic and T. Emery from the Sur laboratory for assistance with Ca²⁺ imaging and A. Heynen from the Bear laboratory for technical advice on the inhibitory avoidance task. We thank all members of the Feng laboratory for their help and support. We thank M. Ball and J. Ball for their insight and inspiration throughout this project. We also thank S.F. Lin and R. Buxton for their support of this research. This work was supported by a grant from Simons Foundation Autism Research Initiative (SFARI Award ID: 307913) to G.F. and M.M.H., NIH grants to G.F. (NIH/NIMH, R01MH097104) and M.M.H. (R01MH107680), and funds from the Poitras Center for Affective Disorders Research and the Stanley Center for Psychiatric Research at the Broad Institute of MIT and Harvard to G.F. M.M.H. is additionally supported by the Brain and Behavior, Sloan, Klingenstein and Feldstein Foundations. M.F.W. is supported by an NIH Ruth L. Kirschstein National Research Service Award (FMH098641A). R.D.W. is supported by the Swiss National Science Foundation.

Author Contributions M.F.W. and G.F. conceived the genetic studies and designed associated experiments; R.D.W. and M.M.H. conceived the physiologic studies and designed associated experiments. All authors designed the behavioural studies. M.F.W. and R.D.W. collected the data. M.F.W., R.D.W. and L.I.S. analysed the data. M.F.W., R.D.W., M.M.H. and G.F. interpreted the results. M.F.W., M.M.H. and G.F. wrote the paper with input from R.D.W.

Author Information Reprints and permissions information is available at www.nature.com/reprints. The authors declare no competing financial interests. Readers are welcome to comment on the online version of the paper. Correspondence and requests for materials should be addressed to G.F. (fengg@mit.edu).

METHODS

***Ptchd1* conditional knockout mice.** *Ptchd1* conditional knockout mice were generated by homologous recombination in R1 embryonic stem cells and implanted in C57Bl/6J blastocysts using standard procedures. The targeting vector was designed to flank exon 2 of the *Ptchd1* gene with *loxP* sites and a neomycin (Neo) selection cassette. Chimaeric mice were crossed to C57Bl/6J females (Jackson Labs). Germline transmission was determined by genotyping PCR of mouse tail DNA, using primer pFW Pt1cKO Gen 1a (5'-GGATGGTACCACCTACAATATGC-3') and pRV Pt1cKO Gen 3b (5'-AAGCCAAAGAGTTTACCCTG-3') for the wild-type allele (187 base pairs (bp)) and the floxed allele (227 bp). The F1 hybrids were crossed to C57Bl/6J β -actin Flp mice to excise the Neo cassette. The floxed mice were then backcrossed to C57Bl/6J mice for five generations. After the fifth generation, speed congenic genotyping PCRs were conducted to determine the approximate purity of the background. Only mice showing >95% C57Bl/6J background were used for subsequent matings. Backcrossed *Ptchd1*-knockout mice were then bred with C57Bl/6J β -actin Cre mice to produce germline knockouts of the floxed allele. Genotypes were determined by PCRs using the pFW Pt1cKO Gen 1a and pRV Pt1cKO Gen 4c (5'-GGACTTGGAGTAAACCACC-3'; in the Neo cassette) primers for the knockout allele (351 bp). For all behavioural experiments in the C57Bl/6J background, *Ptchd1*^{Y⁻} (knockout) and *Ptchd1*^{Y⁺} (wild type) males were bred with *Ptchd1*^{+/+} females. For the C57 and 129 mixed background behavioural experiments, 129 wild-type males were bred with *Ptchd1*^{+/+} C57Bl/6J females and the F1 offspring were used for experiments. Animals were housed 3–5 by genotype per cage at a constant 23 °C in a 12 h light–dark cycle (lights on at 07:00) with *ad libitum* food and water (unless otherwise noted).

Healthy age-matched male mice between 2–5 months were used for all behavioural experiments. Sample sizes were chosen based on standards in the field as well as previous experience with phenotype comparisons. No statistical methods were used to predetermine sample size. All behaviour experiments employed a group counterbalancing strategy to ensure that both genotypes were being tested at equal frequencies throughout the testing day. For drug studies, mice were chosen at random to be included in the vehicle-treated versus drug-treated groups. Experimenters were blind to genotype, but not group (that is, group A versus group B), during data acquisition and analysis. D'Agostino and Pearson omnibus normality tests were run. When normality was violated, non-parametric tests (Wilcoxon rank-sum) were used. ANOVA was used to estimate group variance where multiple comparisons were made. All data analysed with two-tailed *t*-tests showed similar variances between groups. Data presented as scatter plots with mean denoted by bar, unless otherwise noted. All animal experiments were conducted according to the NIH Health Guide for Care and Use of Laboratory Animals and were approved by the Massachusetts Institute of Technology Institutional Animal Care and Use Committee.

***Ptchd1*-YFP mice.** *Ptchd1*-YFP mice were generated by homologous recombination in R1 embryonic stem (ES) cells and implanted in C57Bl/6J blastocysts using standard procedures. The targeting vector replaced exon 1 of the mouse *Ptchd1* gene with ATG-eYFP-STOP cassette and a Neo cassette. Correctly altered ES cell colonies were PCR screened using primers targeting the YFP insert and long-arm PCR (LA Taq) methods. Chimaeric mice were crossed to C57Bl/6J females from Jackson Labs. Germline transmission was assessed through genotyping PCR of mouse tail DNA, using primers pFW Pt1-YFPki Gen 3a (5'-TTACTTCCTTTTCCCACC-3'), pRV Pt1-YFPki Gen 3a (5'-CCCAGTTCTCTAGTAGATTCC-3'), and pFW Pt1-YFPki Gen 3b (5'-GGAGATGAATCTAGGTGGAG-3') for the wild-type allele (positive band, 190 bp) and the YFP positive allele (positive band, 316 bp). The F1 hybrids were backcrossed to C57Bl/6J mice for two generations. Female mice containing the YFP insertion (*Ptchd1*-YFP^{+/+}) were used for all immunohistochemistry experiments.

***In situ* hybridization.** mRNA *in situ* hybridization was performed with 20 μ m cryosections from freshly frozen P0, P15, and P35 brain tissue from male mice using a mixture of two digoxigenin (DIG)-labelled probes against mouse *Ptchd1* cDNA (GenBank Accession NM_001093750.1; ex2 base pairs 372–1006 and ex3 base pairs 1290–2027), except for the wild type and knockout comparisons, in which only the ex2 probe was used. The hybridization signal was detected using an alkaline-phosphatase-conjugated anti-DIG antibody (Roche) and developed using 5-bromo-4-chloro-indolylphosphate/nitroblue tetrazolium (Roche). Sections were imaged using an Olympus BX61 motorized fluorescent microscope.

Immunohistochemistry. Mice were perfused with ice-cold 1 \times PBS and 4% paraformaldehyde. Brains were then fixed overnight at 4 °C before vibratome sectioning. We washed 50 μ m sections with 1 \times PBS for 3 \times 5 min before a 1 h room temperature incubation in blocking solution (5% normal goat serum, 2% BSA, 0.2% Triton X-100 in 1 \times PBS). Sections were then incubated overnight at 4 °C in primary antibody solution: rabbit anti-GFP (Invitrogen A11122; 1:1000), chicken anti-GFP (Abcam 13970; 1:1000), mouse anti-GAD67 (Millipore 5406; 1:1000), rabbit anti-somatostatin (Peninsula Labs T4102; 1:1000), and mouse anti-NeuN

(Millipore MAB377; 1:1000). Following the 3 \times 20 min wash in 1 \times PBS, tissue was incubated for 4 h at room temperature in a second antibody solution: goat anti-rabbit Alexa 488 (LT A-11034; 1:1000), goat anti-rabbit Alexa 555 (LT A-21428; 1:1000), goat anti-mouse Alexa 488 (LT A-11001; 1:1000), goat anti-mouse Alexa 555 (LT A-21422; 1:1000), and goat anti-chicken Alexa 488 (LT A-11039; 1:1000). Sections were once again washed 3 \times 20 min in 1 \times PBS before mounting onto glass slides using Fluoro-Gel. Images were taken with an Olympus Fluoview 1000 confocal microscope. YFP co-labelling was quantified using ImageJ. Images were converted to 8-bit files and automatically background subtracted and thresholded. The resulting images were converted to a mask and then the processes 'fill holes' and 'watershed' were implemented. The processed images were then analysed using the 'analyze particles' feature with the squared size set to '200-Infinity' and the show feature set to 'outlines'. This end product of this procedure was an image containing enumerated cell skeletons. Skeleton images from the green and red channels were merged and overlapping skeletons were counted as a co-labelling event.

Slice electrophysiology. Freshly prepared brain slices from P21–P28 male mice were superfused with oxygenated ACSF (125 nM NaCl, 25 nM NaHCO₃, 25 nM glucose, 2.5 nM KCl, 1.25 nM NaH₂PO₄, 1.2 nM MgCl₂, 2 nM CaCl₂, 1.7 nM ascorbic acid) and recorded at 30–34 °C. Patch pipettes (2.5–4 M Ω) contained the following intracellular solution in 140 nM KMeSO₄, 10 nM KCl, 10 nM HEPES, 0.1 nM EGTA, 4 nM Mg-ATP, 0.2 nM Na-GTP, 10 nM phosphocreatine, (285 nM mOsm, pH 7.2). For rebound burst characterization, cells were held in current clamp at potentials ranging from –85 to –25 mV through constant current injection. Rebound bursting was determined following a 600 ms, –0.5 nA current step. Events crossing two standard deviations of the baseline noise were considered bursts. To determine T and SK currents, responses to different hyperpolarizing steps (500 ms, ranging from –110 to –60 mV) were recorded in voltage clamp configuration. T currents were isolated through application of the SK channel blocker apamin (100 nM), whereas SK currents were estimated by digital subtraction of the isolated T current from control currents without apamin in slices from 4–5 mice per genotype. Cells where the input resistance changed >15% during the recording were excluded from the analysis.

***In vivo* TRN recordings.** Hyperdrives containing 12 individually adjustable microdrives loaded with 1–2 stereotrodes were built as previously described³⁷. Mice were anaesthetized with 1% isoflurane and mounted on a stereotaxic frame. A 3 \times 2.5 mm craniotomy (centre coordinate from bregma, medio-lateral: 2.5 mm, anterior-posterior: –1.3 mm) was drilled and the hyperdrive was implanted at a 15° angle relative to midline. At time of implantation, stereotrodes were lowered <500 μ m into the brain. Three stainless steel screws (one located prefrontal and two cerebellar) served as electroencephalography (EEG) electrodes and ground and anchored together with two additional fixation screws the hyperdrive to the skull. After recovery, mice were connected to a custom-made 64-channel preamplifier headstage (Neuralynx) and data was acquired using a Neuralynx Digilynx recording system. Stereotrode signals were amplified, filtered between 0.1 Hz and 9 kHz and digitized at approximately 30 kHz. Spikes were manually clustered using the MClust toolbox for MATLAB, and bursts were identified as at least two spikes with an inter-spike interval of \leq 10 ms, which were preceded by \geq 70 ms of silence. Spindle detection was performed as previously described¹². The EEG signal was filtered within the spindle frequency band (9–15 Hz) and the Hilbert transform (MATLAB function 'hilbert') was computed. The envelope of the signal (1 s smoothing) was used as a basis for spindle detection. A threshold of one standard deviation (s.d.) was applied and each threshold crossing, with parameters of >0.5 s and <3 s, were initially included. These events were subsequently visually inspected before being included in the analysis. To assess consistency in the phase locking of individual TRN neurons with spindles, we used spike phase synchrony analysis between unit firing and spindle band (9–15 Hz) filtered component of the local field potential (Extended Data Fig. 3d–f). For each TRN unit, we first constructed a spike-phase histogram of firing rates relative to alpha. Units were considered significantly phase-locked if the distribution of spike phases significantly differed from a uniform distribution on the basis of Rayleigh's test for circular uniformity (cut-off, $P < 0.05$). To quantify the degree of phase-locking, the Pearson's correlation coefficient between spike counts and phase angle was computed for each unit. Analysis was performed in MATLAB using the circular statistics toolbox.

Sleep analysis. Sleep-related immobility was used to measure sleep bout duration in mice (C57, $n = 9$ WT and 10 KO; *Sst*-Cre, $n = 10$ WT and 10 KO), a technique that has previously been shown to correlate ($r = 0.94$) with EEG recordings⁵⁰. We used BIOBSERVE Behavioural Sequencer boxes (BIOBSERVE) that utilize Piezo sensors and video recordings to automatically score 23 different movements/behaviours, including immobility (Sequencer label 'still'). The lighting inside the boxes was set to 5–10 lx, which mimicked home cage light intensity in the MIT animal holding facility. Mice were placed into a custom-made transparent plastic cylinder (16 cm diameter \times 16 cm height) containing home cage bedding in order to reduce the arena parameters and facilitate sleep. At 07:00, mice were placed in the

behavioural sequencers and given 1 h to acclimate. After the acclimation period, behaviour was automatically scored for 6 h (08:00–14:00). Data was manually curated to identify bouts of sleep, which were defined as at least 40 s of immobility⁵⁰ that is not interrupted by more than 2 s of upper body movements (sequencer labels 'head', 'face', 'nose', 'cheek', 'back', 'orient_look', 'orient_sniff') or by 4 or more seconds of general body movements (sequencer labels 'paw', 'leg', 'tummy', etc.). These bout parameters were confirmed by two observers viewing raw video during pilot tests. Behavioural recordings and analysis were conducted by a genotype-blind experimenter. Given the 40 s minimum required to be classified as a bout, median data and cumulative probability were used to compare genotypes. Kolmogorov–Smirnov and the Wilcoxon rank-sum tests were used for statistical analysis. All individual data points are plotted with crossbar denoting median.

Fibre-photometry-based optical chloride measurements. Mice ($n = 6$ WT and 6 KO) were injected with 400 nl of AAV-hSyn-SuperClomeleon into the LGN (from Bregma A-P, -2 mm; M-L, -2.1 mm; D-V, -2.5 mm) and chronically implanted with optical fibres (400 μm , Doric lenses) targeted directly above LGN (D-V, 2.1 mm). Following at least two weeks of virus expression, FRET-based measurement of visual-evoked $[\text{Cl}^-]$ responses was performed as previously described¹³. Briefly, CFP excitation was achieved through a fibre-coupled LED (Thorlabs) light source, filtered using a 434 nm clean-up filter (MF434-17 Thorlabs) and light was delivered to the LGN via a 600 μm , 0.48 NA optic patch cord (Fig. 3a) SuperClomeleon CFP and YFP emissions were separated using a single-edge beam splitter (FF511-Di01, Semrock) and collected using a two femtowatt silicon photoreceiver (Newport). Signal was digitized and recorded using a TDT signal acquisition system (Tucker-Davis Technologies). Visual stimulation consisted of a 50 ms LED light pulses delivered to the eye contralateral to the recorded LGN. Normalized delta fluorescence ($\Delta F/F$) was calculated for evoked responses relative to the baseline fluorescence level before each event (1-s window) and smoothed with a convolution filter (50 ms half-width). The minimum signal within a 500 ms window following stimulation was considered the peak response. For pharmacological SK channel enhancement, mice were injected with 25 mg kg^{-1} 1-EBIO following 30 min of baseline recordings. Maximal drug effects were estimated from evoked responses recorded between 30 min to 1 h following injection.

Visual detection task. Mice (C57, $n = 8$ WT and 9 KO from 2 independently tested cohorts; *Sst-Cre*, $n = 8$ WT and 8 KO from 2 independently-tested cohorts; 1-EBIO, 7 WT-Veh, $n = 7$ WT 1-EBIO, 7 KO veh., 7 KO 1-EBIO) were food restricted to 85–90% of their *ad libitum* body weight and training occurred in a custom-built test chamber as previously described³². During testing, a white noise indicated that a new trial was available, and mice had to continuously break an infrared barrier for 500–700 ms to initiate a trial. Upon successful initiation, a 50 ms visual stimulus was presented randomly either on the left or right side. Correct response at the corresponding nose-poke unit resulted in a milk reward (10 μl evaporated milk, Nestle) that was available for 15 s. Following an inter-trial interval of 5 s, a new trial became available. Response at the incorrect location resulted in immediate blockage of poke access and a 30 s timeout before the next trial. To test for distractibility, in one third of the trials a 50 ms distractor appeared at the opposite location of where the stimulus would be displayed in the 200 ms time window before successful initiation. For drug treatment experiments, mice were injected with 1-EBIO (Tocris #1041; 25 mg kg^{-1} in 10% DMSO; subcutaneous injection) or vehicle 30 min before testing. Wilcoxon rank-sum test was used for statistical analysis. All individual data points are plotted with crossbar denoting median.

Fura-2AM calcium imaging. Freshly prepared brain slices from P21–P28 male mice ($n = 4$ WT and 5 KO) were superfused with oxygenated ACSF (125 nM NaCl, 25 nM NaHCO_3 , 25 nM glucose, 2.5 nM KCl, 1.25 nM NaH_2PO_4 , 1.2 nM MgCl_2 , 2 nM CaCl_2 , 1.7 nM ascorbic acid) and recorded at 30–34 °C. Cells ($n = 37$ WT, 36 KO) were filled with Fura-2AM dye (Molecular Probes) using a Picospritzer II that applied ~ 10 pounds per square inch (psi) for 1 min through a 1–2 M Ω glass pipette. Slices were given 1 h to recover in ACSF before imaging. Individual cells were imaged using an Olympus BX61WI microscope with an attached CoolSnapF2 camera. Pixel intensity was measured using ImageJ software with whole-field background correction. Ratiometric values were converted to $[\text{Ca}^{2+}]_i$ using the following equation

$$[\text{Ca}^{2+}]_i = K_d(R - R_{\min}) / (R_{\max} - R) S_{F2} / S_{b2}$$

where K_d refers to the Ca^{2+} dissociation constant (140 nM), R refers to the ratiometric measurement of the observed cell, R_{\max} and R_{\min} correspond to the ratio under conditions of saturated Ca^{2+} levels and in zero Ca^{2+} , respectively. The values of S_{b2} (bound state) and S_{F2} (free Ca^{2+} state) are proportional to the fluorescence excited by 380 nm under conditions of saturated Ca^{2+} levels and in zero Ca^{2+} , respectively. Unpaired t -tests were used to compare nanomolar concentrations between the two groups. Data presented as mean \pm s.e.m.

Open field. Locomotor activity in mice (C57, $n = 30$ WT and 31 KO from 3 independently tested cohorts; mixture of C57 and 129 mice (referred to hereafter as mix), 10 WT and 11 KO from 1 cohort; amphetamine-treated, 5 WT veh., 5 WT amph., 6 KO veh., 6 KO amph.; 1-EBIO, 13 WT veh., 13 WT 1-EBIO, 13 KO veh., and 15 KO 1-EBIO from 2 independently-tested cohorts; *Sst-Cre*, 21 WT and 22 KO from 2 independently tested cohorts) was evaluated over a 60 min period in an automated Omnitech Digiscan apparatus (AccuScan Instruments). Locomotor activity was assessed as total distance travelled (m). Anxiety-like behaviour was defined by number of rearings and time spent in the centre as compared to time spent in the perimeter (thigmotaxis) of the open field. For drug treatment experiments, mice were placed in the open field arena for 30 min before amphetamine (3 mg kg^{-1} in saline; intraperitoneal injection), 1-EBIO (25 mg kg^{-1} in 10% DMSO; subcutaneous injection), or vehicle injections. Mice were then returned to open field arena for an additional 30–90 min. Two-way repeated measures ANOVA with Bonferroni post-hoc tests were used for statistical analysis. Time-binned data ('distance') presented as mean \pm s.e.m. Summated data ('total distance') plotted as individual data points with crossbar denoting mean. One C57 knockout mouse was excluded for escaping from the arena during testing.

Grooming. Young adult male mice (C57, $n = 9$ WT and 13 KO from 1 cohort; mix, $n = 10$ WT and 12 KO from 1 cohort) were used for analysis of grooming behaviour. Individually housed animals were habituated in the testing room for one hour before experimentation. Mice were video-taped for 2 h under 2 lx (red light) illumination. Grooming behaviours were coded from 19:00–21:00 (2 h beginning at the initiation of the dark cycle). This segment was analysed using Noldus Observer software and the total amount of time in the 2 h segment spent grooming was determined. A genotype-blind observer recorded all types of grooming, including incidences of face-wiping, scratching/rubbing of head and ears, and full-body grooming. Two-tailed t -tests were used for statistical analysis. All individual data points are plotted with crossbar denoting mean.

Rotarod. Motor coordination was assessed in mice (C57, $n = 19$ WT and 21 KO from 2 independently tested cohorts; mix, $n = 10$ WT and 10 KO from 1 cohort) using an accelerating rotarod test (Med Associates) over the course of two days. On the first day (training day) animals underwent three 5 min trials at a constant speed (16 r.p.m.). On the second day (testing day), animals underwent three 5 min trials at accelerating speeds (4–40 r.p.m.). For all trials, the latency to fall was determined. Animals were tested for three trials in a single day with an inter-trial interval of 10–30 min. Two-way repeated measures ANOVA with Bonferroni post-hoc tests were used for statistical analysis. Data plotted as mean \pm s.e.m. Two C57 knockout mice were excluded for jumping off the rotarod during testing.

Hanging wire. Mice (C57, $n = 12$ WT and 11 KO from 1 cohort; mix, 10 WT and 12 KO from 1 cohort; 1-EBIO, 6 WT veh., 6 WT 1-EBIO, 6 KO veh., and 6 KO 1-EBIO from 1 cohort; *Sst-Cre*, 12 WT and 11 KO from 1 cohort) were suspended 40 cm above the ground from a 2 mm horizontal wire. The average of three trials with an inter-trial interval of 5 min was recorded. For drug treatment experiments, mice were injected with 1-EBIO (Tocris #1041; 25 mg kg^{-1} in 10% DMSO; subcutaneous injection) or vehicle 30 min before testing. Two-tailed t -tests were used for statistical analysis. All individual data points are plotted with crossbar denoting mean.

Gait. The forepaws of the mice (C57, $n = 10$ WT and 11 KO from 1 cohort) were painted green and the hindpaws were painted pink. After a two minute habituation trial, the mice were allowed to walk down a 50 cm track. The length and width of each stride were measured by an observer blind to genotype and the averages were recorded. Two-tailed t -tests were used for statistical analysis. All individual data points are plotted with crossbar denoting mean.

Hot plate. Mice (C57, $n = 20$ WT and 21 KO from 2 independently tested cohorts; mix, 10 WT and 12 KO from 1 cohort) were placed onto a heating block set to 55 °C surface temperature (Columbus Instruments). Latency to lick a forepaw or hindpaw was measured. The average of three trials with an inter-trial interval of 5 min was recorded. Two-tailed t -tests were used for statistical analysis. All individual data points are plotted with crossbar denoting mean.

Acoustic startle and pre-pulse inhibition. Auditory abilities and sensory motor function in mice (C57, $n = 20$ WT and 21 KO from 2 independently-tested cohorts; mix, 10 WT and 12 KO from 1 cohort) was measured using Hamilton Kinder Scientific Pre-pulse Startle Monitor chambers with Startle Monitor software. On the first day, mice underwent a 5 min acclimation trial in the acoustic startle boxes. On the second day, half of the mice were tested on the acoustic startle protocol while the other half was tested on the pre-pulse inhibition protocol. These protocol groups were switched on the third day. To test acoustic startle, mice are presented with pulses of various decibel levels without pre-pulses for approximately 30 min. The testing session is preceded by a 5 min exposure to 65 dB background noise. Each mouse then receives a total of 92 stimuli (trials) with inter-trial intervals ranging from 7–23 s presented in pseudo-random order. The stimuli include a presentation of eight pulse-alone trials (120 dB, 40 ms pulse, four at the beginning and

four at the end of the session), 77 pulse trials (seven each of 70, 75, 80, 85, 90, 95, 100, 105, 110, 115, and 120 dB, 40 ms pulse), and seven trials each without pulse or pre-pulse presentation. To test pre-pulse inhibition, mice were once again exposed to 65 dB background for 5 min before testing. Each mouse received a total of 57 stimuli (trials) with inter-trial intervals ranging from 7–23 s presented in pseudorandom order. The stimuli include a presentation of eight pulse-alone trials (120 dB, 40 ms pulse, four at the beginning and four at the end of the session), 35 pre-pulse trials (seven each of 70, 75, 80, 85 and 90 dB, 20 ms pre-pulse given 100 ms before a 120 dB, 40 ms pulse), and seven trials each without pulse or pre-pulse presentation. The pre-pulse inhibition percentage within each test session was calculated as follows: $(100 - (\text{mean pre-pulse response}/\text{mean pulse response}) \times 100)$. For all experiments, response to startle stimuli is measured in newtons (N). Startle at each pulse level is averaged across trials and then across animals in a treatment group. Two-way repeated measures ANOVA with Bonferroni post-hoc tests were used for statistical analysis. Data plotted as mean \pm s.e.m.

Three-chambered social interaction assay. Littermate male mice (C57, $n = 10$ WT and 11 KO from 1 cohort; mix, 10 WT and 12 KO from 1 cohort) were used for all tests. Age and size-matched 129 male target subjects ('stranger 1' and 'stranger 2') were habituated to being placed inside wire cages for three days (20 min per day) before beginning of testing. Test mice were habituated to the testing room for at least 1 h before the start of behavioural tasks. The social test apparatus consisted of a transparent acrylic box with removable floor and partitions dividing the box into three chambers. The wire cages used to contain the stranger mice were cylindrical, 11 cm in height, a bottom diameter of 10.5 cm with the bars spaced 1 cm apart (Galaxy Cup, Spectrum Diversified Designs). An inverted metal can was placed on the top of the cage to prevent the test mice from climbing on the top of the wire cage. For the sociability test, the test animal was introduced to the middle chamber and left to habituate for 10 min. Following this period, the middle chamber doors were opened and the test mouse was allowed to freely explore all three chambers for an additional 10 min. The test mouse was then returned to the middle chamber, after which an unfamiliar mouse (stranger 1) was introduced into a wire cage on one of the side-chambers and an empty wire cage (E) on the other side-chamber. The dividers were then raised and the test animal was allowed to freely explore all three chambers over a 10 min session. Following the 10 min session, the mouse was returned to the middle chamber while a novel stranger mouse (stranger 2) was inserted in the wire cage, previously empty, and again the test animal was left to explore for a 10 min session. The time spent by the mouse (nose-point) in close proximity (~ 5 cm) to the wire cages was calculated using automated software (Noldus Ethovision 9). The release of the animals and relative position of social and inanimate targets was counterbalanced. However, for each individual test animal the location of stranger 1 was maintained during stranger-1-E and stranger-1-stranger-2 testing of the social behaviour. One-way ANOVA with Bonferroni multiple comparison tests were used for statistical analysis. All individual data points are plotted with crossbar denoting mean.

Resident intruder. Mice (C57, $n = 10$ WT and 10 KO from 1 cohort; 1-EBIO, 6 WT veh., 6 WT 1-EBIO, 6 KO veh., 6 KO 1-EBIO from 1 cohort; *Sst-Cre*, 6 WT and 6 KO from 1 cohort) were individually housed for 2 weeks before testing with bedding left undisturbed for one week before testing. Animals were tested in a room with 10lx lighting. On the test day, animals were habituated to the test room for 1 h before testing. After acclimation, an age- and weight-matched conspecific male stranger mouse was introduced to the home cage of the test animal. The subsequent interactions were videotaped for 5 min. All interactions were analysed using Noldus Observer by a genotype-blind observer. Aggressive interactions were defined by instances of biting, fighting, and tail-rattling. For drug treatment experiments, mice were injected with 1-EBIO (Tocris #1041; 25 mg kg⁻¹ in 10% DMSO; subcutaneous injection) or vehicle 30 min before testing. Wilcoxon rank-sum and

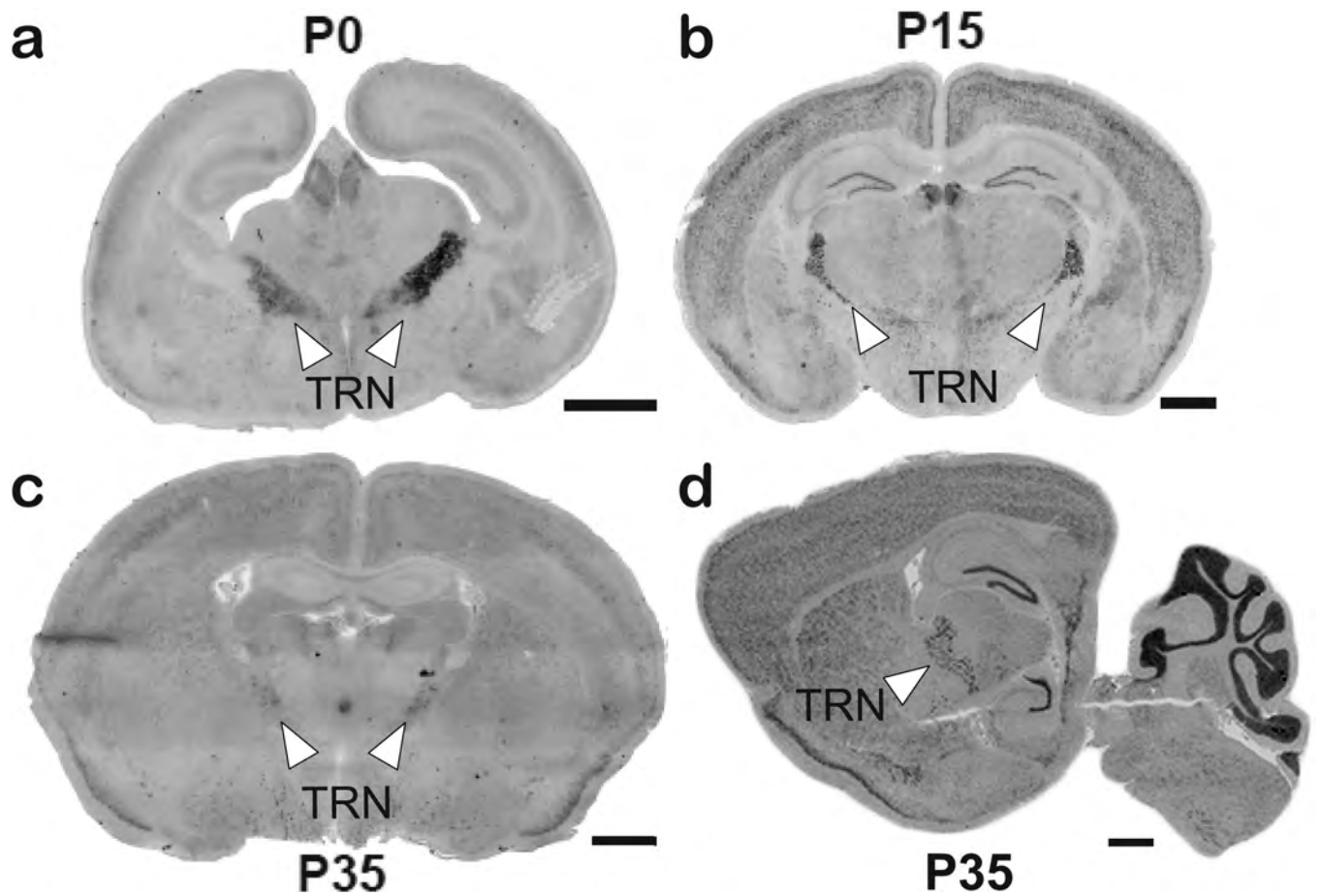
Kruskal–Wallis non-parametric tests were used for statistical analysis because wild-type mice did not pass normality tests. All individual data points are plotted with crossbar denoting median.

Inhibitory avoidance. Mice (C57, $n = 24$ WT and 23 KO from 2 independently-tested cohorts; mix, 10 WT and 12 KO from 1 cohort, 1-EBIO, 7 WT veh., 8 WT 1-EBIO, 9 KO veh., and 10 KO 1-EBIO from 2 independently-tested cohorts; *Sst-Cre*, 11 WT and 12 KO from 1 cohort) underwent one training session followed by 24 h and 48 h post-training trials. On the training day, mice were placed in the light side of the inhibitory avoidance box (Ugo Basile) and allowed to habituate for 30 s. To quantify pre-shock latency and the effects of baseline locomotor activity levels on this task, the door to the dark side of the box was then opened and the latency to cross was measured. Upon entering the dark side of the box, the mice were given a 0.5 mA shock for 2–4 s, followed by a 60 s post-shock habituation. On the probe trials, mice were placed in the light side of the box with the door to the dark side already opened. Latency to cross was once again measured with a maximum duration of 9 min. For drug treatment experiments, mice were injected with 1-EBIO (Tocris #1041; 25 mg kg⁻¹ in 10% DMSO; subcutaneous injection) or vehicle 30 min before the shock training protocol. Two-way repeated measures ANOVA with Bonferroni post-hoc tests were used for statistical analysis. All individual data points are plotted with crossbar denoting mean.

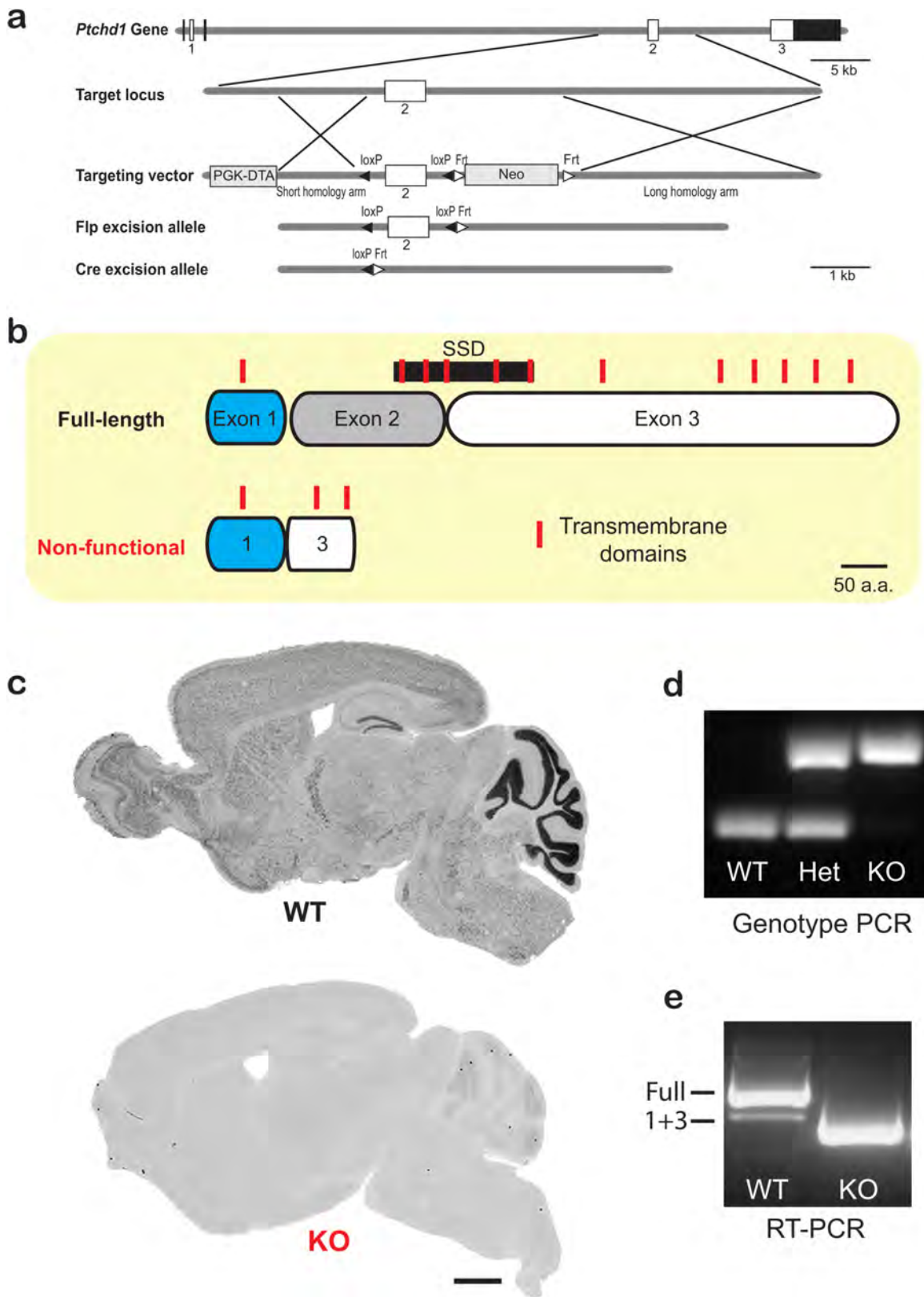
Fear conditioning. Mice (C57, $n = 10$ WT and 11 KO from 1 cohort) were tested for fear-induced freezing using Med Associates fear-conditioning chambers encased in sound attenuating cubicles optimized for near infrared (NIR) video recording. The training protocol involved a 3 min habituation period in the conditioning box, followed by three rounds of a 30 s tone +2 s of 0.75 mA shock +90 s rest. The final shock was followed by a 2 min post-training habituation. The following day, mice were returned to the conditioning box and the time spent freezing was measured. Four hours after, the mice were returned to the conditioning boxes with modifications. A white triangular insert was added to change the dimensions of the box and 0.1% acetic acid was sprayed onto the base of the box in order to change the scent of the box. Once again, the time spent freezing over the course of 5 min was measured. Freezing was measured using Video Freeze software package analysis of NIR recordings. Two-tailed *t*-tests were used for statistical analysis. All individual data points are plotted with crossbar denoting mean.

Morris water maze. Spatial learning testing in mice (C57, $n = 10$ WT and 10 KO from 1 cohort) was conducted using a testing pool that was 120 cm in diameter and a platform 8 cm in diameter. The platform was submerged 1 cm below the water surface. Pool water was maintained at $23.0 \pm 0.5^\circ\text{C}$ and made opaque by mixing in non-toxic white paint. During training, 90 s duration trials were used. If the animals did not find the platform within 90 s, the experimenter guided the animal to the platform. After reaching the platform, the animals were left for 15 s on top of the platform before being removed. Trials were administered for 5–6 days with four trials per animal per day with the platform located in the north-west (NW) quadrant. For two consecutive days after the training protocol, 60 s probe trials were performed (one per day). The reversal training commenced with the platform in the south-east quadrant, and proceeded as described above. The experimenter followed the animals' progress using tracking software outside of the testing room. Tracking and analysis were performed using the Noldus Ethovision software. Two-way repeated measures ANOVA with Bonferroni post-hoc tests and one-way ANOVA with Bonferroni multiple comparison tests were used for statistical analysis. All individual data points are plotted with crossbar denoting mean.

50. Fisher, S. P. *et al.* Rapid assessment of sleep-wake behavior in mice. *J. Biol. Rhythms* **27**, 48–58 (2012).

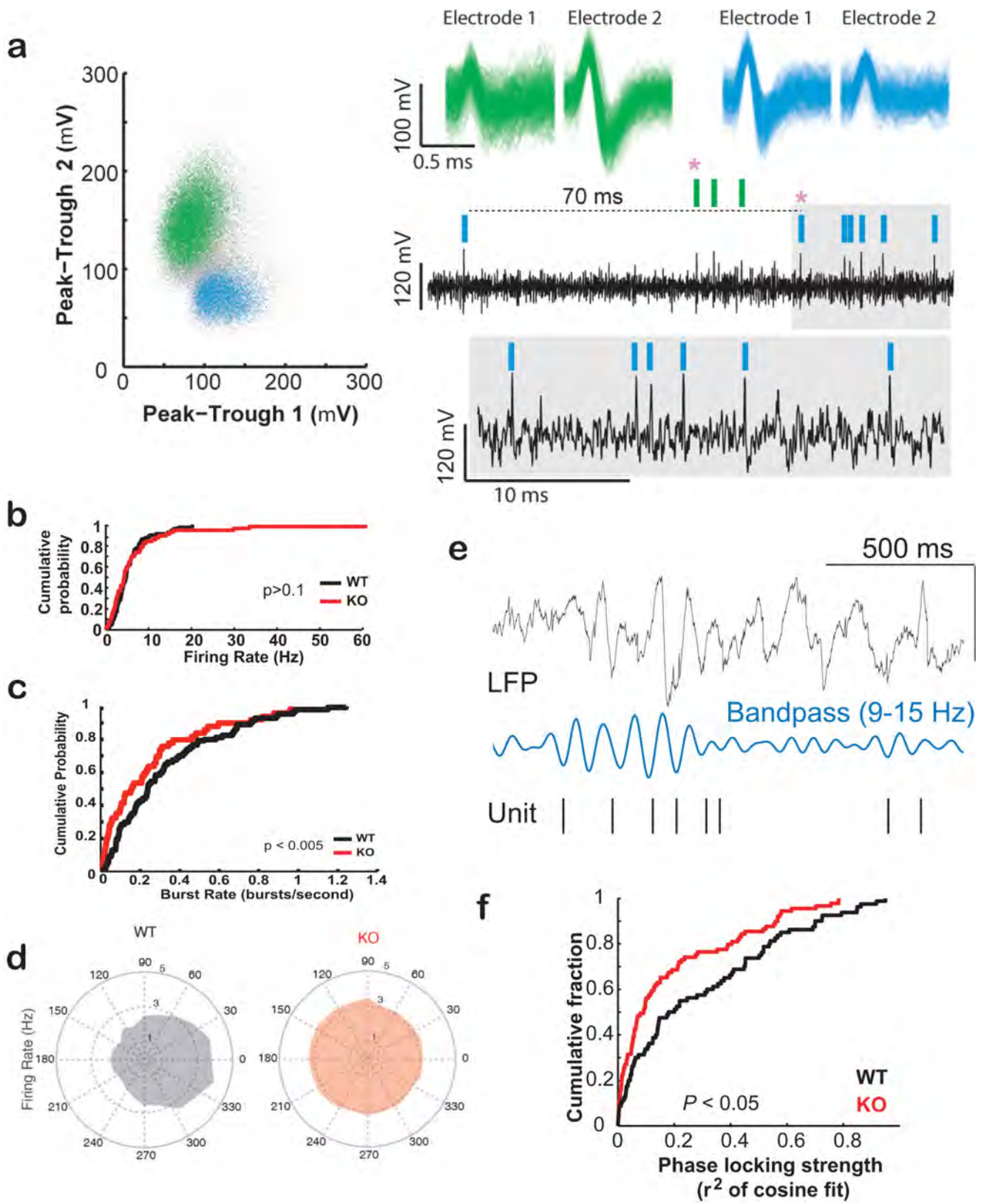


Extended Data Figure 1 | Developmental expression pattern of *Ptchd1*. a–d, *In situ* hybridization labelling of *Ptchd1* mRNA at P0 (coronal) (a), P15 (coronal) (b), and P35 (coronal and sagittal) (c–d) from 3 C57/Bl6 wild-type mice per age. White arrows indicate location of TRN region (scale bars, 1 mm).



Extended Data Figure 2 | Generation of *Ptchd1*-knockout mouse.
a, Schematic describing strategy to create *Ptchd1*-knockout mouse. Mice containing targeted allele were crossed to β -actin Flp mice to remove the Neo cassette and β -actin Cre mice to excise exon 2. **b**, Diagram depicting the 'full-length' and non-functional 'exons 1+3' *Ptchd1* isoforms. Genetic ablation of Exon 2 results in the removal of a majority of the

transmembrane domains normally present in the endogenous full-length isoform. **c**, *In situ* hybridization probes targeting exon 2 confirm successful genetic ablation of full-length *Ptchd1* mRNA (scale bar, 1 mm). **d**, PCR genotyping confirms deletion of exon 2 from genome of male knockout mice. **e**, qPCR of wild-type and knockout cDNA samples shows removal of full-length *Ptchd1* isoform. Het, heterozygous.

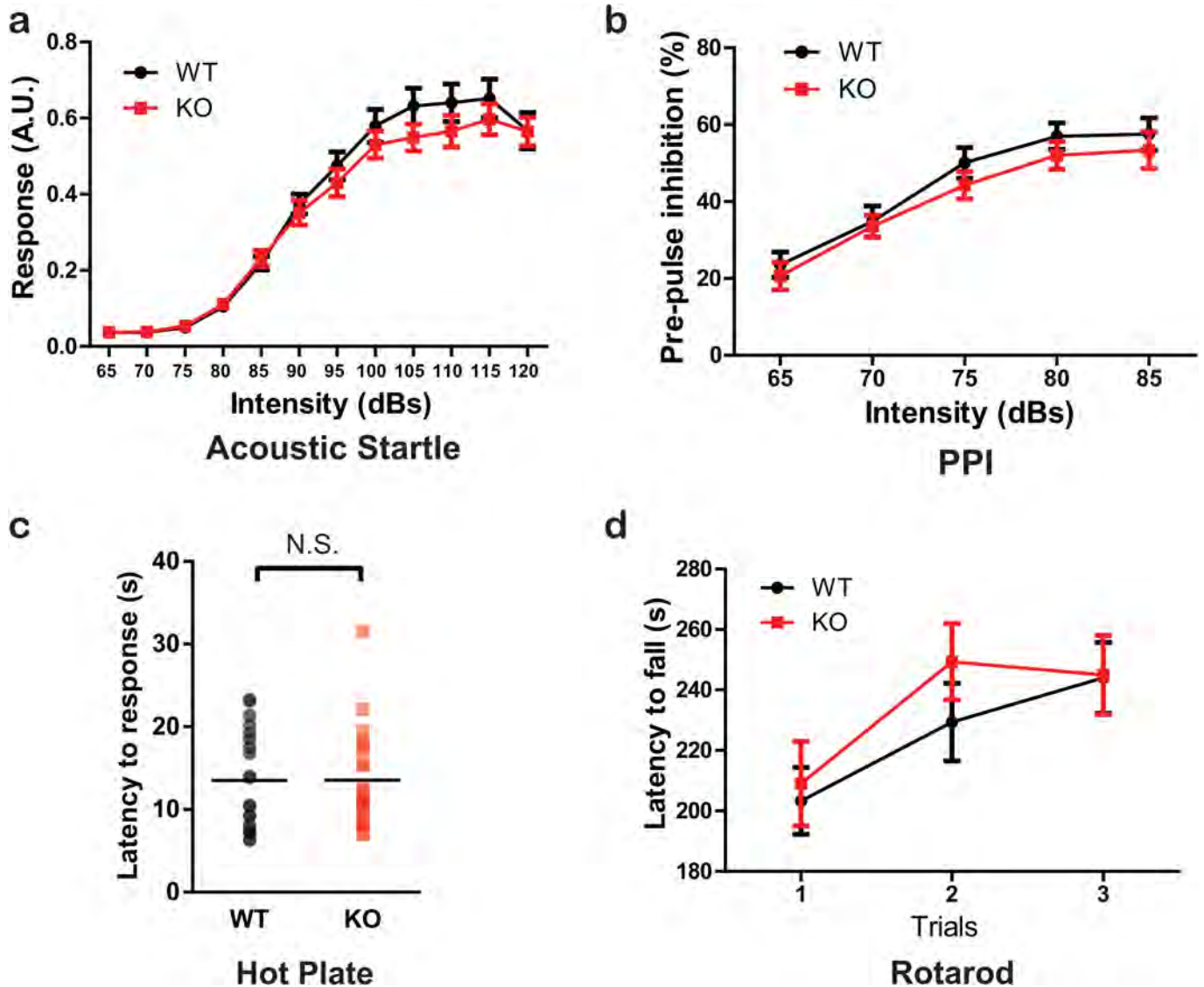


Extended Data Figure 3 | See next page for caption.

Extended Data Figure 3 | Burst and spindle phase-locking characteristics of *Ptchd1*-knockout and wild-type TRN neurons

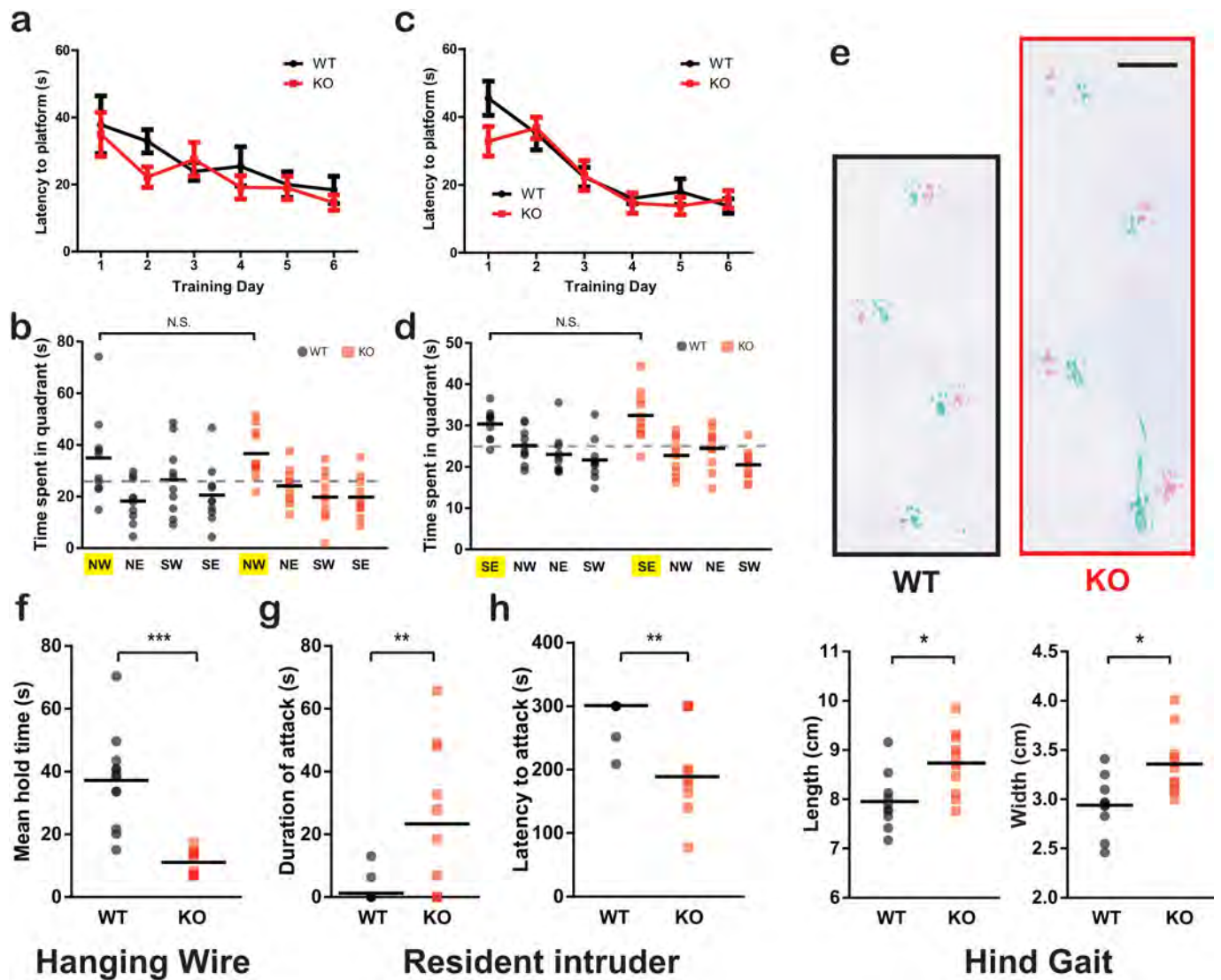
in vivo. **a**, Left, example of unit clustering for a stereotrode recording. Two units (green and blue) are clearly separated when plotting peak-trough of the two electrodes of the stereotrode against each other. Right, spike-wave form of the two clustered units as they appear on the two electrodes of the stereotrode. Raw trace below shows a burst discharge (asterisk) of each unit during non-rapid eye movement sleep with coloured ticks indicating corresponding individual spikes. A burst was identified as at least 2 spikes with an inter-spike interval of ≤ 10 ms, preceded by a period of 70 ms silence. Enlarged trace shows the accelerando-decelerando firing pattern characteristic for a TRN burst. **b**, Firing rate during non-rapid eye movement sleep is comparable between genotypes ($n = 89$ WT,

80 KO cells from 4 WT, 3 KO mice; $P > 0.1$, Kolmogorov–Smirnov test). **c**, *Ptchd1*-knockout TRN neurons show reduced propensity to generate bursts, even when excluding the 10% of knockout cells with the highest firing rate ($n = 89$ WT, 72 KO cells from 4 WT, 3 KO mice; $P < 0.05$, Kolmogorov–Smirnov test). **d**, Spindle-phase histogram for an example wild-type and knockout neuron. Note, the wild-type neuron shows a preferred phase around the peak (0 degrees) of the spindle oscillation in wild type but not knockout. **e**, Example local field potential recording (LFP; top) showing the temporal alignment of TRN spikes (bottom) to the preferred phase of the spindle activity (9–15 Hz, middle). **f**, *Ptchd1*-knockout mice show reduced phase-locking strength to spindle activity compared to wild-type littermates ($n = 89$ WT, 80 KO cells from 4 WT, 3 KO mice).



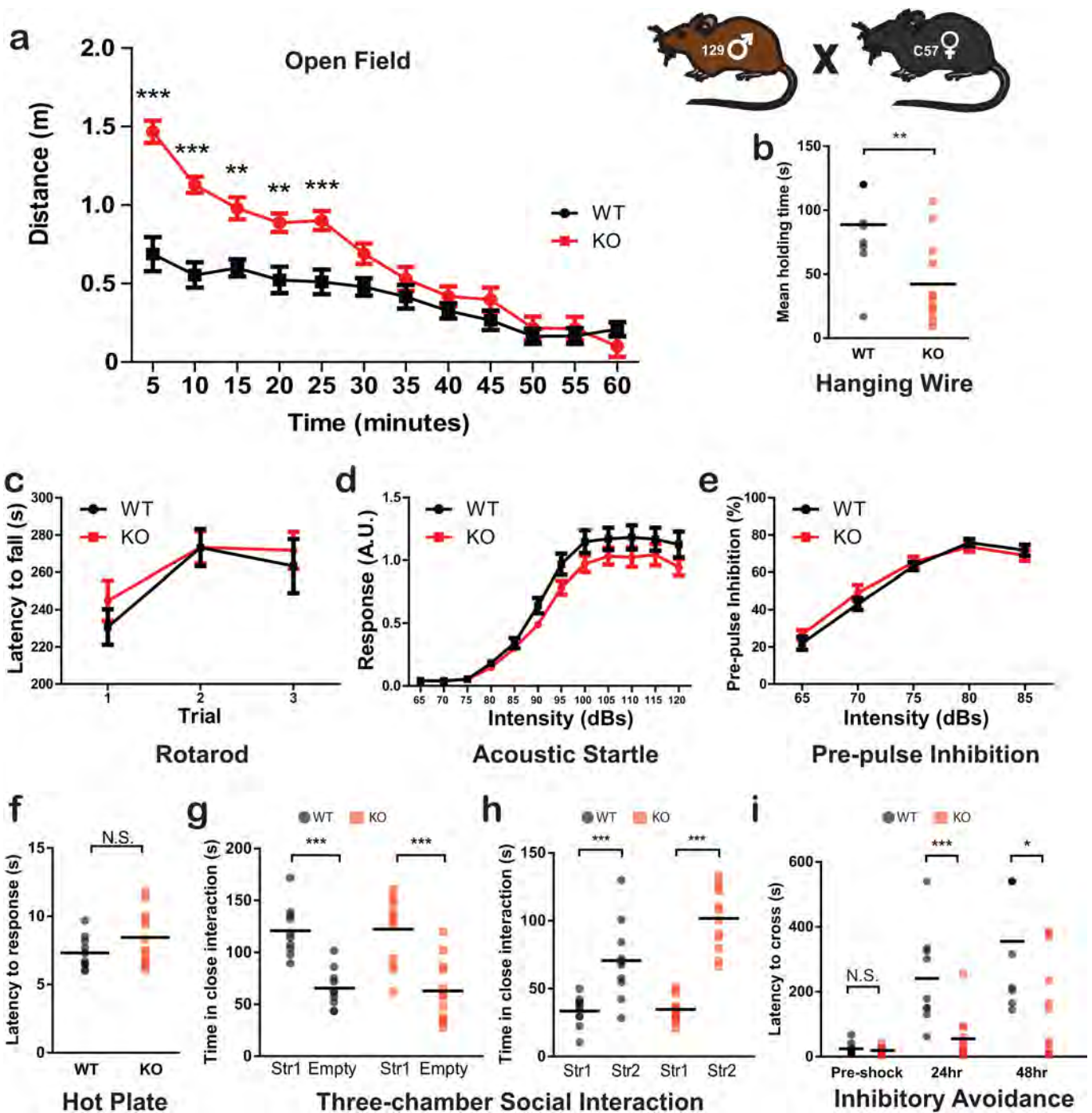
Extended Data Figure 4 | *Ptchd1*-knockout mice have intact sensory responses and rotarod performance. a–c, Normal acoustic startle (a), pre-pulse inhibition (PPI; b) and hot plate response (c) in *Ptchd1*-knockout mice ($n = 20$ WT (a–c), 20 KO (b), 21 KO (c)). d, *Ptchd1*-

knockout mice show normal motor coordination on the accelerating rotarod test ($n = 19$ WT, 20 KO). Two-tailed *t*-tests (c) and two-way repeated measures ANOVA with Bonferroni post-hoc tests (a–b, d) were used for statistical analysis. Error bars, mean \pm s.e.m. NS, not significant.



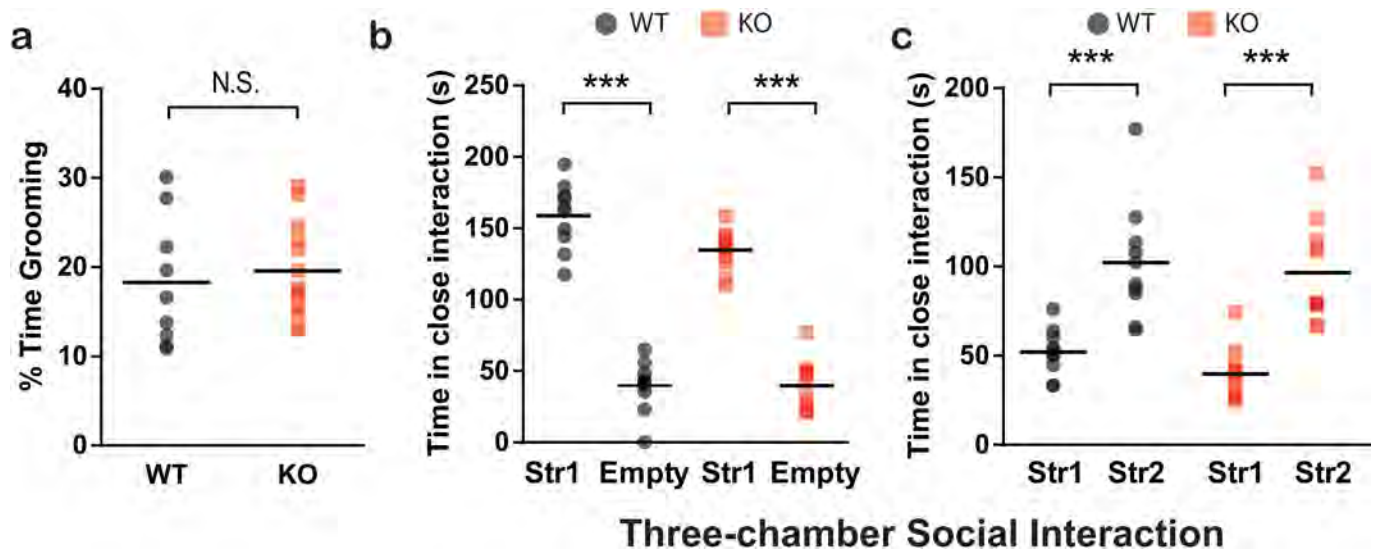
Extended Data Figure 5 | Intact spatial learning but motor and aggression abnormalities in *Ptchd1*-knockout mice. **a**, Comparable learning curves between wild-type and knockout mice during cued training protocol. **b**, Intact spatial learning demonstrated in 24h probe trial. **c**, *Ptchd1*-knockout mice show normal reversal learning curve. **d**, No significant difference between wild-type and knockout mice in 24h probe trial after reversal learning protocol ($n = 10$ WT, 10 KO). **e**, Representative images of wild-type (black) and knockout (red) strides. Forepaw position is represented by green paint and hindpaw position is represented by pink paint (scale bar, 2 cm). Quantification reveals elongated stride length and width ($n = 10$ WT, 11 KO). **f**, Knockout mice show marked reductions in

grip strength as measured by the hanging wire test ($n = 12$ WT, 11 KO). **g**, **h**, Knockout mice attack intruder mice for a longer duration (**g**) and with a shorter latency to attack (**h**) in the resident-intruder test for aggression ($n = 10$ WT, 10 KO). Two-way repeated measures ANOVA with Bonferroni post-hoc tests (**a**, **c**), one-way ANOVA with Bonferroni multiple comparison tests (**b**, **d**), two-tailed *t*-tests (**e**, **f**) and Wilcoxon rank-sum tests (**g**, **h**) were used for statistical analysis. Chance performance (25%) represented by dashed grey lines (**b**, **d**). Error bars, mean \pm s.e.m (**a**, **e**); mean (**b**, **d**, **e-f**), median (**g**, **h**). * $P < 0.05$; ** $P < 0.01$; *** $P < 0.001$.



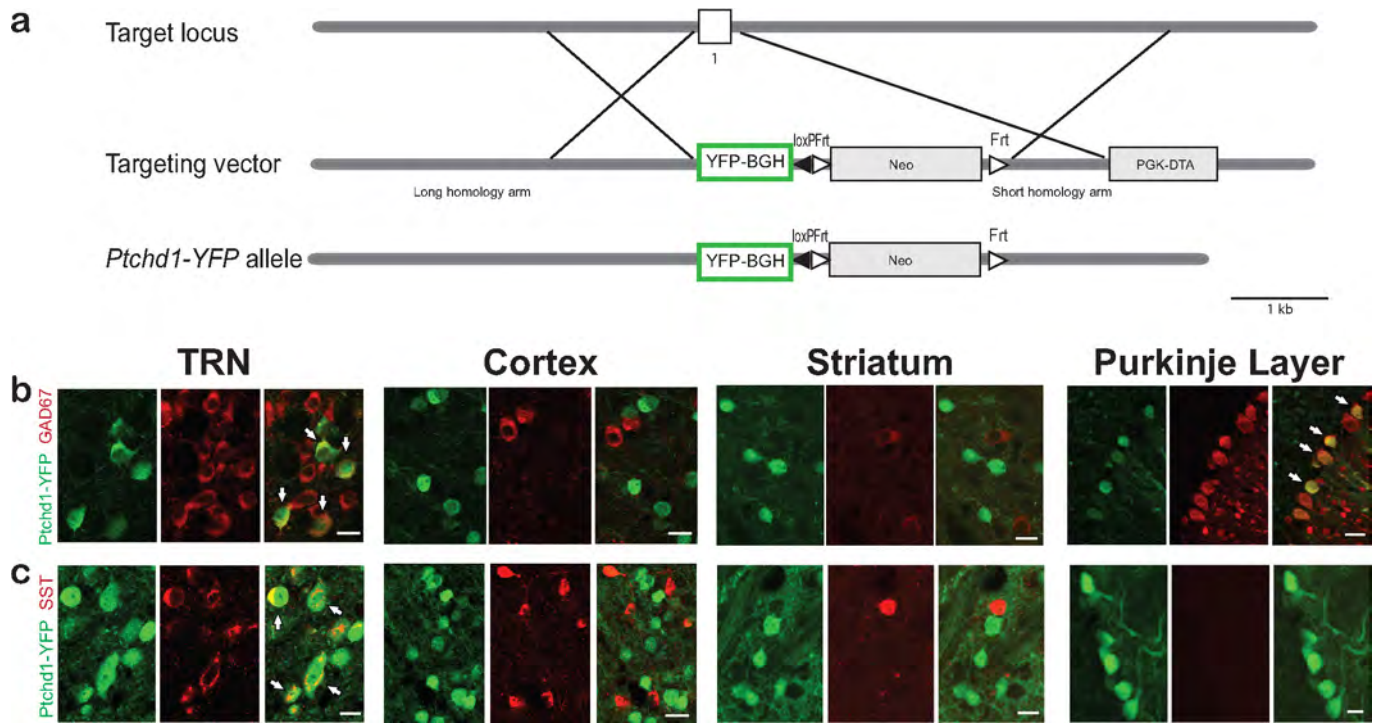
Extended Data Figure 6 | Hyperactivity, hypotonia, and learning deficits in C57/129 *Ptchd1*-knockout mice. a, *Ptchd1*-knockout mice showed increased locomotor activity ($n = 10$ WT, 11 KO). b, c, Knockout mice show decreased mean holding time in the hanging wire test (b) ($n = 10$ WT, 12 KO), but normal motor coordination in the rotarod task (c) ($n = 10$ WT, 10 KO). d–f, Sensory responses as measured by acoustic startle (d), pre-pulse inhibition (e), and hot plate (f) are also normal in knockout mice ($n = 10$ WT, 12 KO). g–h, Normal sociability (g) and novel

social recognition (h) in mixed background *Ptchd1*-knockout mice ($n = 10$ WT, 11 KO). i, Knockout mice show impaired associative learning and memory in the inhibitory avoidance task ($n = 9$ WT, 12 KO). Two-tailed t -tests (b, f), one-way ANOVA with Bonferroni multiple comparison tests (g, h), and two-way repeated measures ANOVA with Bonferroni post-hoc tests (a, c–e, i) were used for statistical analysis. Error bars, mean \pm s.e.m.; horizontal bars, mean (b, f–i). * $P < 0.05$; ** $P < 0.01$; *** $P < 0.001$.



Extended Data Figure 7 | Normal grooming and social interaction behaviours in *Ptchd1*-knockout mice. **a**, Knockout mice do not show excessive or injurious grooming behaviours ($n = 9$ WT, 13 KO). **b**, **c**, Knockout mice spent comparable amounts of time interacting with stranger mice in the three-chambered social interaction task (**b**) and

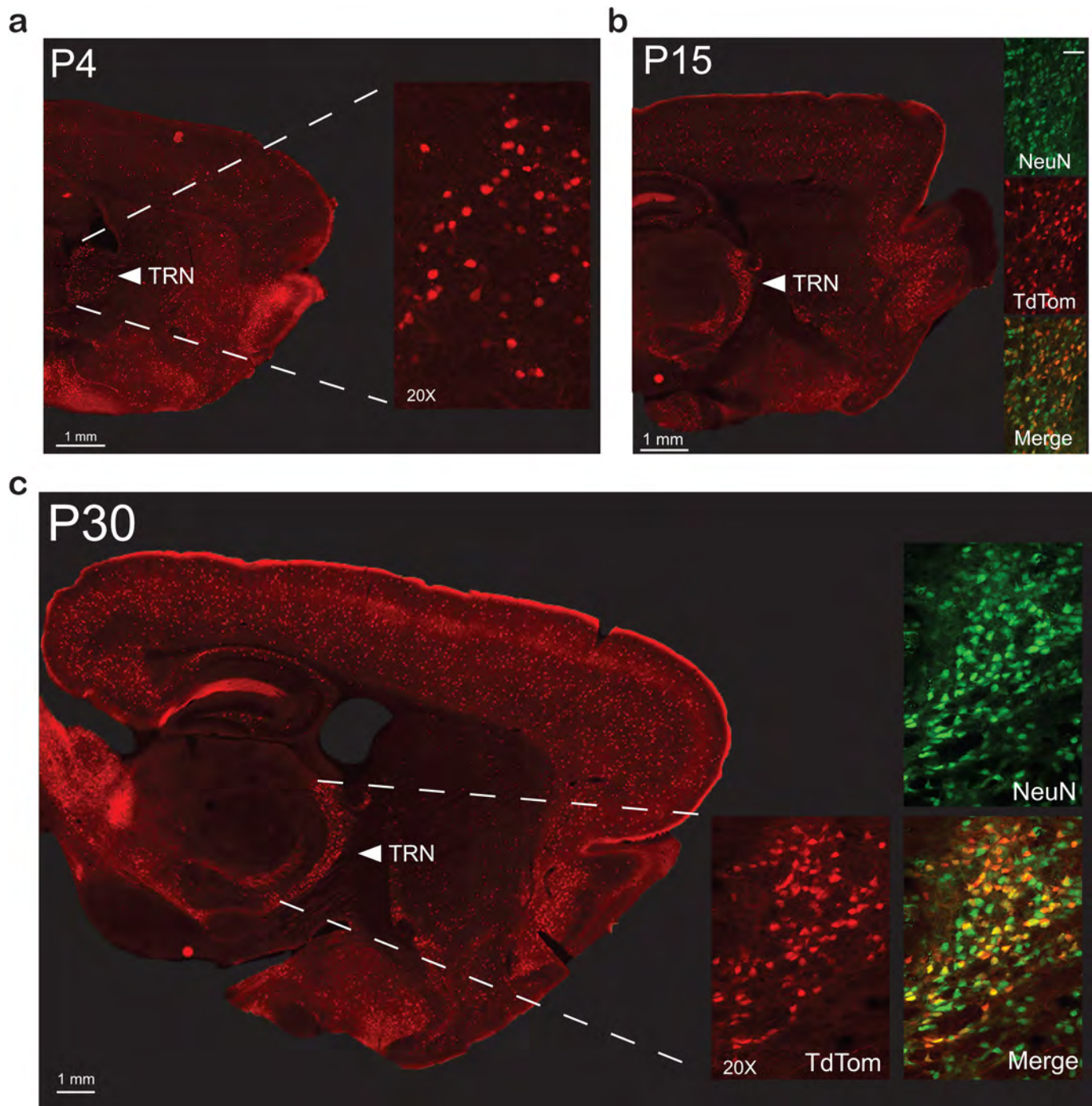
display normal social novelty behaviours (**c**) ($n = 10$ WT, 11 KO). Two-tailed t -tests (**a**) and two-way repeated measures ANOVA with Bonferroni post-hoc tests (**b**, **c**) were used for statistical analysis. Horizontal bars, mean. *** $P < 0.001$.



Extended Data Figure 8 | YFP overlap with somatostatin interneuron marker is primarily confined to the TRN in *Ptchd1*-YFP mice.

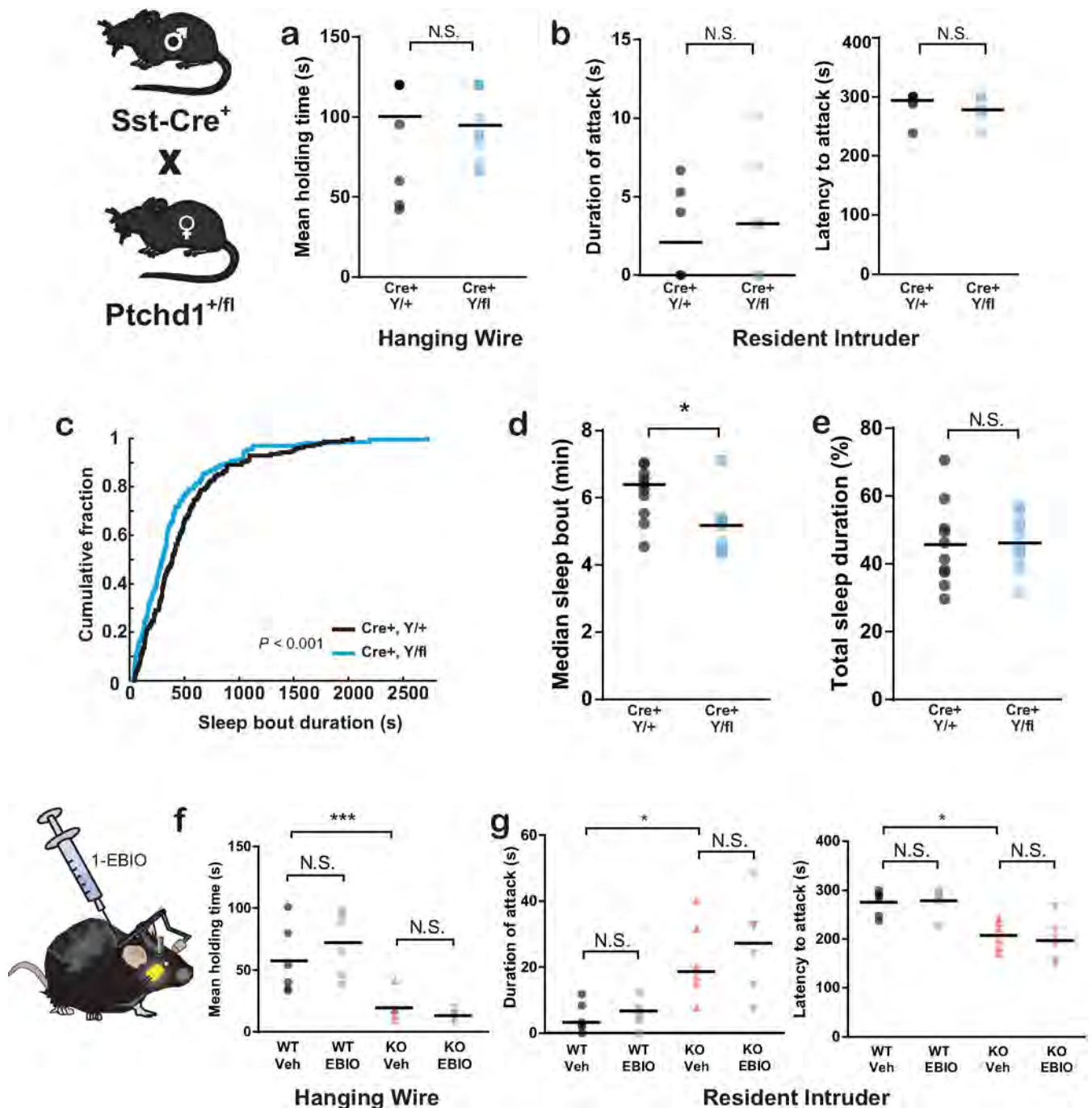
a, Schematic describing strategy to create *Ptchd1*-YFP mouse in which exon 1 was replaced with a YFP-bovine growth hormone poly-A tail

(BGH) cassette. **b**, YFP⁺ cells co-label with anti-GAD67 antibody in TRN and the Purkinje layer of the cerebellum, but not in cortex or striatum. **c**, YFP⁺ cells also co-label with anti-somatostatin antibody in TRN, but not in other structures. Arrows denote overlap. Scale bars, 20 μm.



Extended Data Figure 9 | *Sst*-Cre recombinase activity is early and robust in TRN neurons. **a**, The progeny of *Sst*-Cre⁺ mice crossed to mice showing Cre-dependent expression of the TdTomato fluorescent protein (*Sst*-Cre⁺ TdTomato⁺) show TdTomato⁺ cells in the TRN at P4. Inset

shows magnified image taken with 20× objective. **b, c**, At P15 (**b**) and P30 (**c**), Cre recombinase activity in the TRN of the *Sst*-Cre⁺ TdTomato⁺ mice brains is robust, as shown by the inset depicting the significant TdTomato overlap with the pan-neuronal marker NeuN.



Extended Data Figure 10 | Genetic disruption of *Ptchd1* TRN expression affects sleep stability but not grip strength or aggressive behaviours. **a, b**, *Sst-Cre⁺ Ptchd1^{Y/f}* mice appear normal in the hanging wire (**a**) ($n = 12$ *Ptchd1^{Y/+}*, 11 *Ptchd1^{Y/f}*) and resident intruder task (**b**) ($n = 6$ *Ptchd1^{Y/+}*, 6 *Ptchd1^{Y/f}*). **c–e**, *Sst-Cre⁺ Ptchd1^{Y/f}* mice show reductions in sleep bout duration as shown in cumulative probability plot and comparison of medians (**d**) with no differences in total time spent sleeping when compared to *Sst-Cre⁺:Ptchd1^{Y/+}* littermates (**e**)

($n = 10$ *Ptchd1^{Y/+}*, 10 *Ptchd1^{Y/f}*). **f, g**, 1-EBIO treatment has no effect on performance on the hanging wire (**f**) or resident intruder task (**g**) ($n = 6$ WT veh., 6 WT 1-EBIO, 6 KO veh., 6 KO 1-EBIO). Kolomgorov–Smirnov test (**a**), Wilcoxon rank-sum tests (**b, c**), two-tailed *t*-tests (**d**), and two-way repeated measures ANOVA with Bonferroni post-hoc tests (**f**), and Kruskal–Wallis with Dunn’s multiple comparisons tests were used for statistical analysis. Horizontal bars, median (**b, c, e–g**), mean (**d, f**). * $P < 0.05$; ** $P < 0.01$; *** $P < 0.001$.